

A Satellite Study of Tropical Moist Convection and Environmental Variability: A Moisture and Thermal Budget Analysis

HIROHIKO MASUNAGA

Hydrospheric Atmospheric Research Center, Nagoya University, Nagoya, Japan

(Manuscript received 5 October 2012, in final form 21 February 2013)

ABSTRACT

The thermodynamic variability associated with moist convection over tropical oceans is analyzed by making use of a variety of satellite sensors including radars, an infrared and microwave sounder unit, and a microwave radiometer and scatterometer aboard different platforms. Satellite measurements of atmospheric parameters including air temperature, water vapor, cumulus cloud cover, and surface wind are composited with respect to the temporal lead or lag from Tropical Rainfall Measuring Mission (TRMM)-detected convection to obtain statistically continuous time series on hourly to daily time scales. The Atmospheric Infrared Sounder (AIRS)-observed temperature and humidity profiles, representing cloud-cleared sounding, are combined with semi-theoretical estimates of in-cloud temperature and humidity to construct the large-scale mean field. Those measurements are ingested to the moisture and thermal budget equations integrated vertically over each layer separated by cloud base. This strategy makes it possible to evaluate the free-tropospheric (FT) convergence of moisture and dry static energy and their vertical flux at cloud base from satellite observations alone. The main findings include the following: 1) vertical moisture transport at cloud base is the dominant source of FT moistening prior to isolated cumulus development while overwhelmed by horizontal moisture convergence for highly organized systems; 2) FT diabatic heating is largely offset on an instantaneous basis; and 3) FT moistening by convective eddies amounts to a half of the total cloud-base moisture flux in the background state, while large-scale mean updrafts modulate the variability of cloud-base flux when highly organized systems develop. The known correlation between congestus clouds and FT moisture before deep convection may be accounted for by large-scale mean moisture updraft rather than congestus eddy moistening.

1. Introduction

Despite the long established understanding that moist convection is a key ingredient in the dynamics of tropical atmosphere (Riehl and Malkus 1958), a number of outstanding issues have challenged our efforts to fully understand the physics governing tropical convective clouds and their environment. Convective processes and large-scale environment are technically (and often conceptually) difficult to explicitly deal with at the same time because of the vast temporal and spatial gaps lying in between. In practice, the “unresolved” effects of convective processes can be diagnosed with large-scale mean parameters under a certain closure constraint sought by means of a moisture and thermal budget

analysis (Yanai et al. 1973; Arakawa and Schubert 1974). Pioneering observational work in this field typically relies on a relatively limited number of opportunities provided by intensive field campaigns to obtain a full spectrum of meteorological parameters (e.g., Reed and Recker 1971; Yanai et al. 1973; Nitta and Esbensen 1974; Johnson 1976; Thompson et al. 1979; Luo and Yanai 1984; Lin and Johnson 1996). The present work shares scientific interests with these earlier studies but explores a different approach based exclusively on satellite observations instead of ground observational networks.

Recent progress in satellite sensor technology, exemplified by hyperspectral sounders and cloud and precipitation radars among others, has significantly expanded the capability of atmospheric observations from space. Satellite observations provide full global coverage over a long period of time, far beyond the reach of individual field campaigns. There are, however, a few major challenges to the utility of satellite remote sensing

Corresponding author address: Hirohiko Masunaga, Hydrospheric Atmospheric Research Center, Nagoya University, Furocho, Chikusa-ku, Nagoya 464-8601, Japan.
E-mail: masunaga@hyarc.nagoya-u.ac.jp

in light of the present research goals. First, low Earth-orbiting (LEO) satellites, flying over a given geographical location twice or three times at best per day, are so limited in sampling frequency that it is difficult to monitor hourly to subdaily scale variability critical of moist convective processes. This limitation is unavoidable when the analysis involves the LEO sensors that do not currently have any substitute instrument in the geostationary orbit (microwave and active sensors, for instance). Some past work has addressed this problem in a statistical space by projecting many LEO observations onto a composite time axis constructed against an independent infrared or rainfall dataset (Kondo et al. 2006; Zelinka and Hartmann 2009; Mapes et al. 2009) or another LEO satellite (Masunaga 2012a,b). Our strategy here is a direct extension of the method proposed by Masunaga (2012a). Second, thermal emissions from hydrometeors degrade or totally disable infrared soundings of temperature and humidity in cloudy skies. The lack of measurements within clouds can be a serious obstacle, particularly when the effects of convective clouds on atmospheric thermodynamics are of central interest. This paper explores a semitheoretical approach where a hypothetical adiabatic air parcel is combined with the ambient air soundings to obtain in-cloud estimates.

Third, no satellite instrument in operation remotely measures wind except near the sea surface, where scatterometer measurements are available. The divergence terms in the thermal and moisture budget equations would remain undetermined without the knowledge of wind observations. The lack of wind observations from space can be compensated for by prescribed assumptions provided by offline cloud model simulations as implemented in existing satellite algorithms for convective heating (Tao et al. 2006, and references therein). This study, in contrast, pursues a somewhat different goal without the help of any external knowledge of dynamic environment. Instead of deriving a full vertical structure of the heating source and moisture sink, a simplified tropospheric model is used here that consists of two layers separated by cloud base, and the divergence terms in each layer are deduced from observable quantities under the heat and water budget constraints.

A relevant research topic of interest is the potential roles of congestus clouds in free-tropospheric (FT) moistening. Growing evidence appears to suggest the FT moisture control on convection as implied by observations (Numaguti et al. 1995; Yoneyama and Fujitani 1995; Brown and Zhang 1997; Sherwood 1999; Holloway and Neelin 2009), theoretical work (Raymond 2000), and cloud-resolving model simulations (Derbyshire et al. 2004; Takemi et al. 2004). Being a key member in the family of tropical convection along with shallow

cumulus and deep convection (Johnson et al. 1999), congestus clouds have gained increasing attention as a possible driver of the FT moistening that creates an environment favorable for convection to intensify. The transition from congestus to deep convection appears to accompany a deepening of the moist FT layer during a cycle of equatorial waves and the Madden-Julian oscillation (MJO) (Takayabu et al. 1996; Kemball-Cook and Weare 2001; Straub and Kiladis 2003; Mapes et al. 2006). It is less evident whether the congestus moistening is a universal effect that leads to convective deepening even without the aid of wave dynamics. Few studies, with some exceptions (Kuang and Bretherton 2006; Waite and Khouider 2010; Hohenegger and Stevens 2013), have been targeted specifically on the physical processes controlling congestus moistening and the resultant deepening of convection. Waite and Khouider (2010) found that congestus moistening offers a plausible mechanism for preconditioning deep convective development, while Hohenegger and Stevens (2013) argued otherwise based on a variety of evidence.

The main objectives of this study are 1) to develop an analysis method to derive the short-term variability of large-scale mean temperature and humidity from multisatellite observations, 2) to carry out a moisture and thermal budget analysis involving the development of different types of convective systems, and 3) to discuss the observational implications for relevant issues including FT congestus moistening. Data and analysis methods are described in section 2, and the observed thermodynamic variability is shown in section 3. The strategy and results of the budget analysis are presented in section 4, followed by section 5, where the current findings are discussed. The conclusions are summarized in section 6.

2. Data and method

a. Satellite instruments and data products

Satellite instruments involved in the current analysis are summarized in Fig. 1. A precipitating cloud is defined to be present where flagged as “rain certain” in the Tropical Rainfall Measuring Mission (TRMM) Precipitation Radar (PR) level 2 products (TRMM PR Team 2005). Satellite sensors of central importance for this work besides the TRMM PR are the Atmospheric Infrared Sounder and Advanced Microwave Sounder Unit (AIRS/AMSU, hereafter AIRS collectively) and the Advanced Microwave Scanning Radiometer for Earth Observing System (AMSR-E), both carried by the *Aqua* satellite. Cloud-cleared air temperature and vapor mixing ratio are obtained from the AIRS level 2 Standard

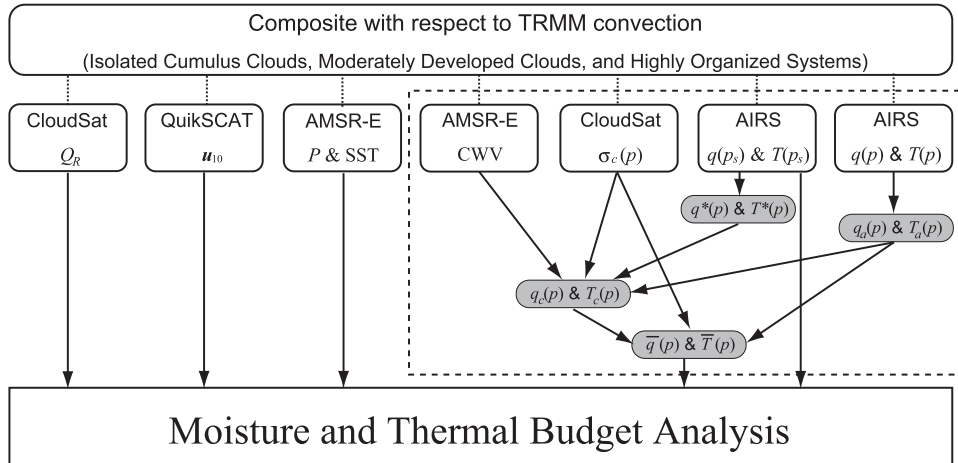


FIG. 1. Analysis flowchart. Dashed box indicates the algorithm to estimate the large-scale mean thermodynamic field (section 3a), where individual humidity and air temperature estimates are shown by shaded boxes. See text for details.

Physical Retrieval (AIRX2RET) version 5 dataset (Susskind et al. 2003, 2011). AMSR-E column water vapor (CWV) and sea surface temperature (SST) are provided by the Remote Sensing Systems (RSS) (Wentz and Meissner 2000). AMSR-E precipitation is retrieved by the Goddard Profiling (GPROF) 2010 algorithm (Kummerow et al. 2001) and is employed for composite surface precipitation in the budget analysis described later. The *CloudSat* Cloud Profiling Radar (CPR) Cloud Classification (2B-CLDCLASS) (Wang and Sassen 2001) and Fluxes and Heating Rates (2B-FLXHR) (L'Ecuyer and Stephens 2003; L'Ecuyer et al. 2008) products are employed for cumulus cloud cover and radiative heating rate, respectively. Near-surface wind vector is obtained from the Quick Scatterometer (QuikSCAT) SeaWinds level 3 daily gridded data (Perry 2001). *Aqua* and *CloudSat* are part of the Afternoon Train (A-Train) constellation and have overpasses around 0130 and 1330 local time (LT), while the QuikSCAT satellite had been flying in a morning (evening) sun-synchronous orbit fixed around 0600 (1800) LT until it ceased to operate in November 2009. Local time of TRMM observations varies from orbit to orbit.

The footprint size varies from sensor to sensor: 4.3 km at nadir for the PR, 13.5 km at nadir for the AIRS, 74 km \times 43 km (6.4 GHz) to 6 km \times 4 km (89 GHz) for the AMSR-E, 1.7 km \times 1.3 km for the *CloudSat* radar, and 37 km \times 25 km for the QuikSCAT scatterometer. The diversity in spatial resolution among different satellite instruments would lead to a systematic inconsistency in instantaneous measurements on a footprint scale. This issue is greatly alleviated in the current analysis since all the parameters are averaged over a common large-scale domain, as noted later.

Pressure levels are chosen to match the AIRS data product, except for the bottom two levels that are the surface and cloud base. Cloud-base pressure p_{CB} is defined at the lifting condensation level (LCL) computed from the observed surface air temperature and humidity. Surface pressure p_s and cloud-base pressure each vary with space and time. While the AIRS product contains air temperature just above the surface, the lowermost vapor mixing ratio in the AIRS dataset is the layer average between 1000 and 925 hPa, and it could be considerably smaller than the surface value. The AIRS lowermost vapor estimate is thus extrapolated down to the surface, assuming a prescribed lower-tropospheric thermodynamic structure typical of a cloud-topped boundary layer over tropical oceans [see appendix of Masunaga (2012a) for details]. Pressure levels farther above are fixed at 925, 850, 700, 600, 500, 400, 300, 250, 200, 150, and 100 hPa. Surface pressure is interpolated to AIRS footprints internally in the AIRS operational algorithm from the National Centers for Environmental Prediction (NCEP) Global Forecast System (GFS) forecast.

Observations over global tropical oceans (15°S–15°N) are analyzed. Continents and islands are all excluded because passive sensor measurements tend to be degraded or unavailable over land. The analysis period spans 7 yr from 1 December 2002 to 30 November 2009, except for *CloudSat*, where the period is 3 yr and 5 months from 1 July 2006 to the same ending date.

b. Composite analysis method

The temporal variability associated with convective development is obtained by the composite analysis method devised by Masunaga (2012a), with minor updates as outlined below. The basic idea is to combine two

LEO satellites flying in different orbits, the *Aqua* and TRMM, for example, and composite observations with respect to the overpass time difference. Air temperature and water vapor measurements from the *Aqua* AIRS are recorded every time when the TRMM PR reports an occurrence of convection nearby sometime before or after. Each AIRS measurement is sorted by the observational time difference and geographical distance from the TRMM-detected convection. The time difference drifts randomly from one overpass to another since the TRMM satellite, flying in a sun-asynchronous orbit, intersects the sun-synchronous *Aqua* orbit at an irregular time interval. AIRS measurements collected over a period of time would thus eventually include numerous samples having a series of different lags or leads from the TRMM and would yield a statistically continuous time sequence of air temperature and water vapor prior and subsequent to convection when averaged together in each time bin. Each snapshot in composite space constitutes a vertical–horizontal cross section, where the horizontal dimension is composited from a series of distance bins circled around the convection. The TRMM PR is insensitive to small cloud droplets but measures precipitation with rain rates higher than $\sim 0.7 \text{ mm h}^{-1}$ (Kummerow et al. 1998). The base point, or the zero on the time and distance axes in composite space, therefore represents the occurrence of precipitating clouds such as cumuli congestus, cumulonimbi, and nimbostratus.

AMSR-E, *CloudSat*, and QuikSCAT data are also composited similarly against the TRMM-detected convection in order to obtain a whole spectrum of environmental variables. QuikSCAT wind vector is projected into two-dimensional local polar coordinates when composited, where the radial axis is defined along the direction from the TRMM-detected convection with outward positive. The radial component is stored for calculating the subcloud-layer divergence. QuikSCAT scalar wind is averaged separately in composite space for use by evaporation and sensible heat flux estimates. The composite time series of all parameters are smoothed over time by ± 2 -h running mean to filter out high-frequency noise irrelevant to the present analysis.

Observations sampled for the composite analysis are broken down by the population density of TRMM convection, hereafter the TRMM precipitation coverage, defined by the number of raining PR pixels across the surrounding $1^\circ \times 1^\circ$ domain. The TRMM precipitation coverage serves as an index of the degree of convective organization as demonstrated by Masunaga (2012b). Figure 2 shows the vertical structure of *CloudSat* cumulus cloud cover (defined below) composited separately for three ranges of the TRMM precipitation coverage of 0%–25%, 25%–50%, and 50%–100%. The

left column is the composite time series while the right column is the vertical–horizontal cross sections at time zero. Cumulus cloud cover is the area fraction occupied by stratocumulus (Sc), cumulus congestus (Cu), nimbostratus (Ns), or deep convective clouds as identified in the *CloudSat* CLDCLASS product. These cloud types are selected as the key players of moist convection with the root on the planetary boundary layer.

When the TRMM precipitation coverage is smaller than 25%, composite clouds are mostly shallow cumuli having tops around 2 km and hardly grow vertically beyond the middle troposphere even at time zero (Fig. 2a). Cumulus cloud cover stays as small as 0.3, varying little over distance (Fig. 2d). This category thus appears to consist of isolated cumulus clouds not standing out much above the background shallow cumuli. The opposite extreme may be seen for TRMM precipitation coverages exceeding 50% (Figs. 2c,f). In this case cumulus cloud towers penetrate the entire troposphere and develop into a horizontally extensive structure over a few hundred kilometers at the time of peak convection ($t = 0$). Highly organized clouds such as mesoscale convective systems (MCSs) are a plausible candidate for this category. The middle row (Figs. 2b,e) is an intermediate class in between, where a systematic vertical and horizontal development is clearly visible, but a majority in this class does not reach as high as the tropopause. The three composite categories may be thus termed as *isolated cumulus clouds* (TRMM precipitation coverage $< 25\%$), *moderately developed clouds* (25%–50%), and *highly organized systems* ($> 50\%$). This terminology is used for labeling each composite category in the remainder of this paper.

The three composite categories may seemingly correspond to shallow cumulus, cumulus congestus, and cumulonimbus (Johnson et al. 1999) as far as the vertical cloud extent is concerned. In reality, the degree of horizontal organization also systematically varies among different categories. In light of a cloud classification employed by recent satellite studies (Romatschke and Houze 2010; Rasmussen and Houze 2011), moderately developed clouds may contain more “wide convective cores” than isolated cumuli and highly organized systems would likely include a majority of “broad stratiform regions.” A one-to-one comparison in terms of cloud morphology is, however, difficult since each composite category, unlike existing snapshot-based categorizations, consists of a full time series where the spatial structure of a cloud system changes over its life cycle. The current terminology therefore only designates the most representative convective system of each category, while different types of cloud systems may coexist during the course of evolution in the composite statistics.

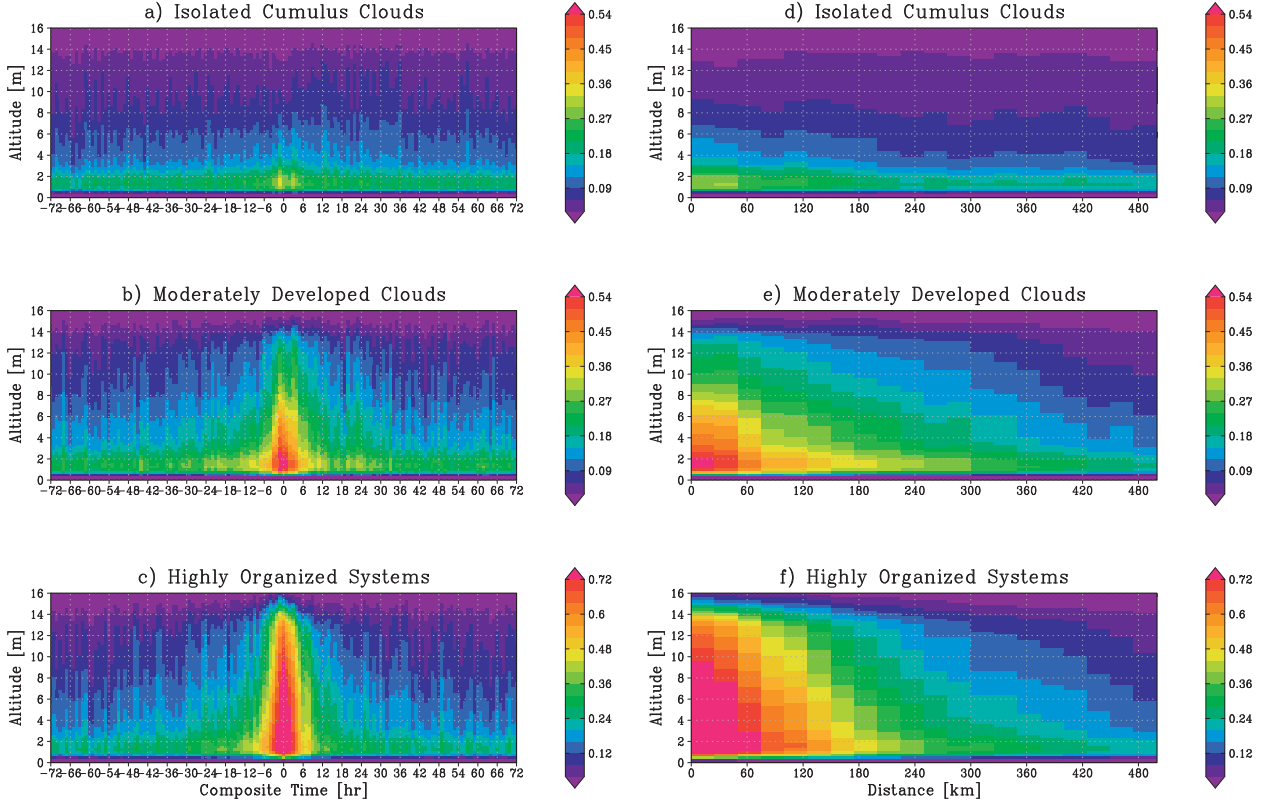


FIG. 2. The composite time series of cumulus cloud cover at distance zero ($R = 0$) for (a) isolated cumulus clouds, (b) moderately developed clouds, and (c) highly organized systems in the z - t plane. (d)–(f) As in (a)–(c), but for the vertical–horizontal (z - R) cross section at time zero.

3. Thermodynamic variability

This section presents the strategy to evaluate large-scale mean temperature and water vapor fields and demonstrates its application to the composite analysis.

a. Synthesis of large-scale mean fields

The utility of infrared sounding is limited where clouds are present. Although the operational AIRS product does not attempt to retrieve temperature and water vapor inside clouds, it uses a stochastic algorithm to obtain cloud-cleared soundings in partially cloudy columns in attempt to minimize the clear-sky bias (Susskind et al. 2003, 2011). The previous approach (Masunaga 2012a), where the AIRS $1^\circ \times 1^\circ$ gridded product was adopted as it is, is updated in this paper to combine the AIRS measurements with a separate estimate of in-cloud vapor and temperature to construct the “all sky” thermodynamic field averaged over a large-scale domain of $O(100\text{ km})$. The analysis procedure is described below.

Figure 1 outlines the analysis flowchart, where the algorithm module illustrated in this section is indicated

by the dashed box. Large-scale mean air temperature and vapor mixing ratio, $\bar{T}(p)$ and $\bar{q}(p)$, respectively, are defined as

$$\begin{aligned}\bar{T}(p) &= \frac{1}{\pi R^2} \int_0^R \hat{T}(p, r) 2\pi r dr \\ \bar{q}(p) &= \frac{1}{\pi R^2} \int_0^R \hat{q}(p, r) 2\pi r dr,\end{aligned}\quad (1)$$

where r denotes the distance axis in composite space, R is the radius of a circular large-scale domain, and p designates the pressure coordinate. All-sky temperature and vapor mixing ratio, denoted by \hat{T} and \hat{q} , respectively, are a weighted average of in-cloud properties, T_c and q_c , and the ambient air properties outside cloud cells, T_a and q_a , as

$$\hat{T}(p, r) = \sigma_c(p, r) T_c(p, r) + [1 - \sigma_c(p, r)] T_a(p, r) \quad (2)$$

and

$$\hat{q}(p, r) = \sigma_c(p, r) q_c(p, r) + [1 - \sigma_c(p, r)] q_a(p, r), \quad (3)$$

where σ_c is the cumulus cloud cover (see section 2b and Fig. 2). The vertical dimension in the *CloudSat* measurements of σ_c is converted from the altitude to pressure coordinates using the AIRS geopotential (described later in this section). Note that all composite variables are a function of time, but the argument t is omitted from the equations for brevity.

The ambient air properties (T_a and q_a) are as provided by the AIRS data product. On the other hand, in-cloud temperature and water vapor are difficult to evaluate directly from satellite measurements. The current strategy is to combine a semitheoretical estimate of temperature and vapor mixing ratio for a saturated air parcel, T^* and q^* , with the ambient air properties to characterize the in-cloud thermodynamic state as

$$T_c(p, r) = \gamma_c(p, r)T^*(p, r) + [1 - \gamma_c(p, r)]T_a(p, r) \quad (4)$$

and

$$q_c(p, r) = \gamma_c(p, r)q^*(p, r) + [1 - \gamma_c(p, r)]q_a(p, r). \quad (5)$$

A hypothetical undiluted air parcel, initially given the observed temperature and vapor mixing ratio of $T_a(p_s, r)$ and $q_a(p_s, r)$,¹ is lifted dry-adiabatically from the surface to cloud base, beyond which $T^*(p, r)$ and $q^*(p, r)$ are calculated following the moist adiabat until the level of neutral buoyancy is reached. The dilution fraction γ_c in (4) and (5) takes into account the entrainment of dry ambient air into the cloud in an idealized manner as

$$\frac{[1 - \gamma_c(p, r)]q_a(p, r)}{\gamma_c(p, r)q^*(p, r)} = \zeta_c(r)\epsilon_c(p, r),$$

or equivalently,

$$\gamma_c(p, r) = \frac{q_a(p, r)}{q_a(p, r) + \zeta_c(r)\epsilon_c(p, r)q^*(p, r)}, \quad (6)$$

where

$$\epsilon_c(p, r) = \begin{cases} -\frac{1}{\sigma_c} \frac{\partial \sigma_c}{\partial z} & \text{for } \frac{\partial \sigma_c}{\partial z} < 0 \\ 0 & \text{otherwise} \end{cases} \quad (7)$$

is an approximate measure of entrainment rate and ζ_c is a proportionality constant independent of height (but allowed to vary horizontally). In-cloud vapor mixing ratio is considered in (6) and (7) to be diluted with the

ambient air at the rate of how rapidly cumulus cloud cover decays over height. The entrainment is assumed to be negligible when cumulus cloud cover does not decrease upward. The parameter ζ_c , having the dimension of length, by definition represents the vertical scale over which a diluted portion of the cloud air evaporates out as it ascends. It would be safe to assume that ζ_c is vertically constant to the extent that such mixing processes may be considered to rely on general aerodynamic properties insensitive to altitude, although this simplification is yet to be verified elsewhere.

The above set of equations constitutes a closed system to yield \bar{q} and \bar{T} once ζ_c is known. The computational procedure begins with an arbitrary guess of ζ_c , with which a tentative estimate of \hat{q} is obtained from (3) and (5)–(7). The initial trial of ζ_c is then adjusted to the additional constraint of

$$\text{CWV}(r) = \int_0^{p_s} \hat{q}(p, r) \frac{dp}{g}, \quad (8)$$

where CWV is given by AMSR-E observations and g is the gravitational acceleration. The equality in (8) is justified by the fact that microwave radiometry, unlike infrared sounding, has sensitivity to in-cloud water vapor as well as to the ambient moisture field. The solutions of ζ_c and \hat{q} are updated iteratively until (3) and (5)–(8) are all satisfied. Once ζ_c is finalized, \bar{T} and \bar{q} are evaluated from (1).

Geopotential, required later to evaluate dry static energy (DSE), is derived from AIRS temperature and water vapor (for virtual temperature) through the hypsometric equation. The hypsometric equation is not applied to T_c and q_c inside clouds where the hydrostatic assumption may be invalid. Instead, the in-cloud and ambient pressures are assumed to be locally equalized at any height above cloud base as is often done in a parcel model, in which case a geopotential surface is horizontal across cloud boundaries. The composite AIRS geopotential $\varphi(p, r)$ thus may be interpolated into clouds as it is and averaged straightforwardly into the large-scale mean $\bar{\varphi}(p)$.

All parameters are binned every 1 h over time and every 25 km over the radius in composite space. This radial bin size is chosen so that each bin contains at least several AIRS 13.5-km footprints, but at the same time is not so large as to smear out the radial gradient of composite parameters (see Fig. 2 for a rapid change of σ_c over radius). To calculate large-scale means, the integral over radius in (1) is replaced by summation as

$$\overline{[\dots]} \equiv \frac{1}{R^2} \int_0^R [\dots] 2r dr = \frac{1}{R^2} \sum_{i=1}^N [\dots]_{i-(1/2)} (r_i^2 - r_{i-1}^2), \quad (9)$$

¹Note that $\hat{T} = T_a$ and $\hat{q} = q_a$ below cloud base, where σ_c vanishes by definition.

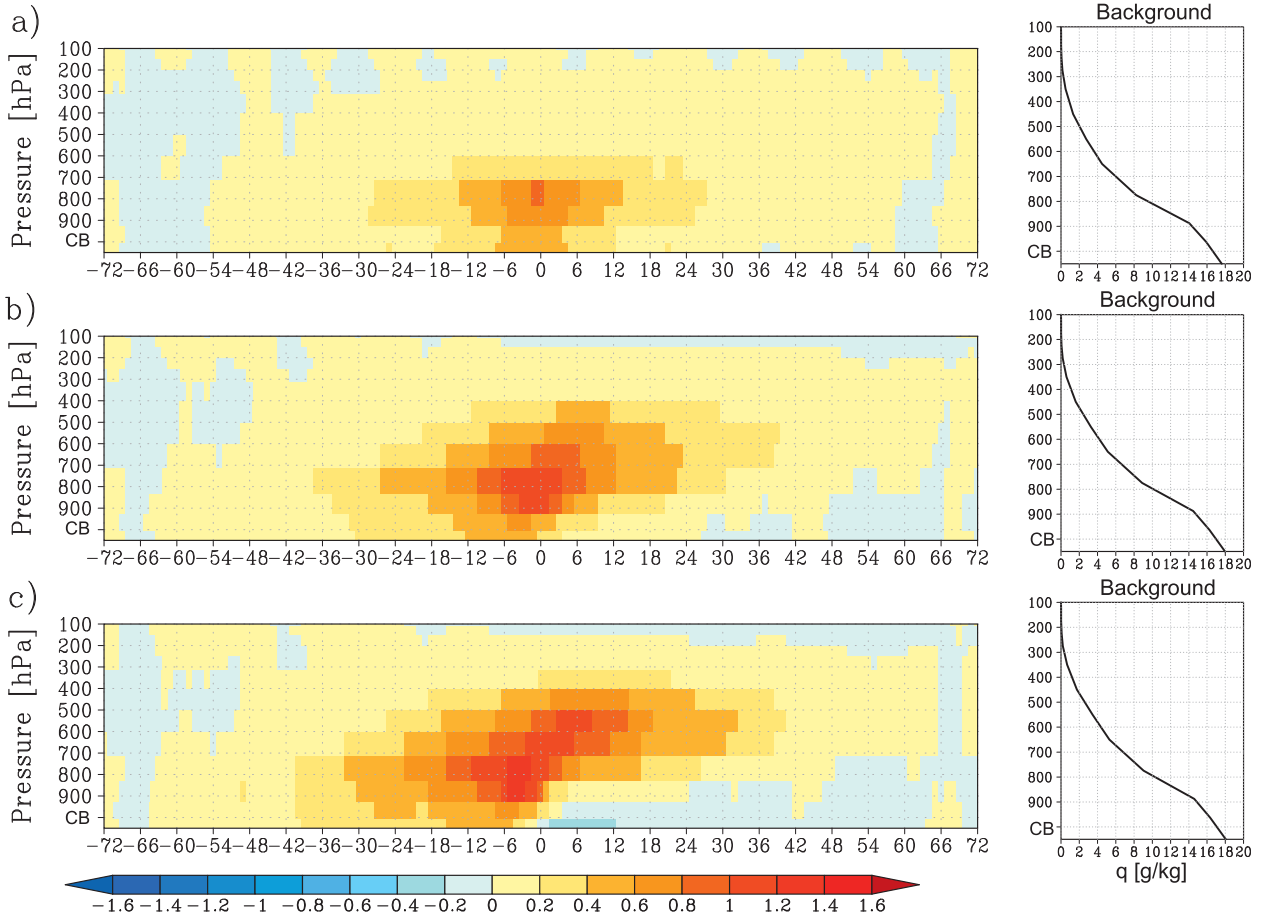


FIG. 3. The time–pressure cross section of large-scale mean vapor mixing ratio (\bar{q}) anomaly (g kg^{-1}) in composite space for (a) isolated cumulus clouds, (b) moderately developed clouds, and (c) highly organized systems (see section 2b for definition). The bottom two layers are partitioned by cloud base or LCL where labeled by CB on the pressure axis. The anomaly is color shaded against the background fields given on the right side computed by temporally averaging the first and last 12-h time series (-72 to -60 h and $+60$ to $+72$ h) together.

where $r_0 = 0$, $r_N = R$, and $[\dots]_{i-(1/2)}$ designates the average within a 25-km ring bound by r_{i-1} and r_i . The large-scale domain size is chosen to be $R = 100$ km throughout this paper. Increasing R would reduce the amplitude of variability in the composite parameters but not qualitatively alter the results.

The large-scale mean thermodynamic field is often replaced by the ambient sounding under the assumption of $\sigma_c \ll 1$. Cumulus cloud cover may be negligibly small when averaged over a time much longer than the lifetime of individual cloud systems, but σ_c is by no means small even in a 100-km scale mean at instances when vigorous convective systems develop as one can see in Figs. 2e and 2f. At the same time, σ_c never reaches unity and the ambient sounding is always available in composite space, although instantaneous AIRS observations are totally contaminated by clouds from time to time. Both the in-cloud and ambient terms in (2) and (3) are therefore retained throughout this paper.

b. Composite vapor mixing ratio and dry static energy

The composite large-scale mean vapor mixing ratio \bar{q} is plotted for different convective systems in Fig. 3. Color shaded are the anomalies of \bar{q} against the background field, which is defined as the temporal mean of the first and last 12-h sequences combined together and shown in panels on the right. A moistening prior to convection ($t = 0$) in the lower free troposphere is visible for all types of convective systems, with a larger magnitude for more-developed systems. The moistening is limited to below the middle troposphere for isolated cumulus clouds, while the moist layer thickens farther upward into the upper troposphere when convection is organized and grows deep. A well-known vertical tilt is evident in vapor mixing ratio anomaly for highly organized systems, that is, upper-tropospheric moisture does not reach the maximum until when the lower troposphere begins to dry just after convection

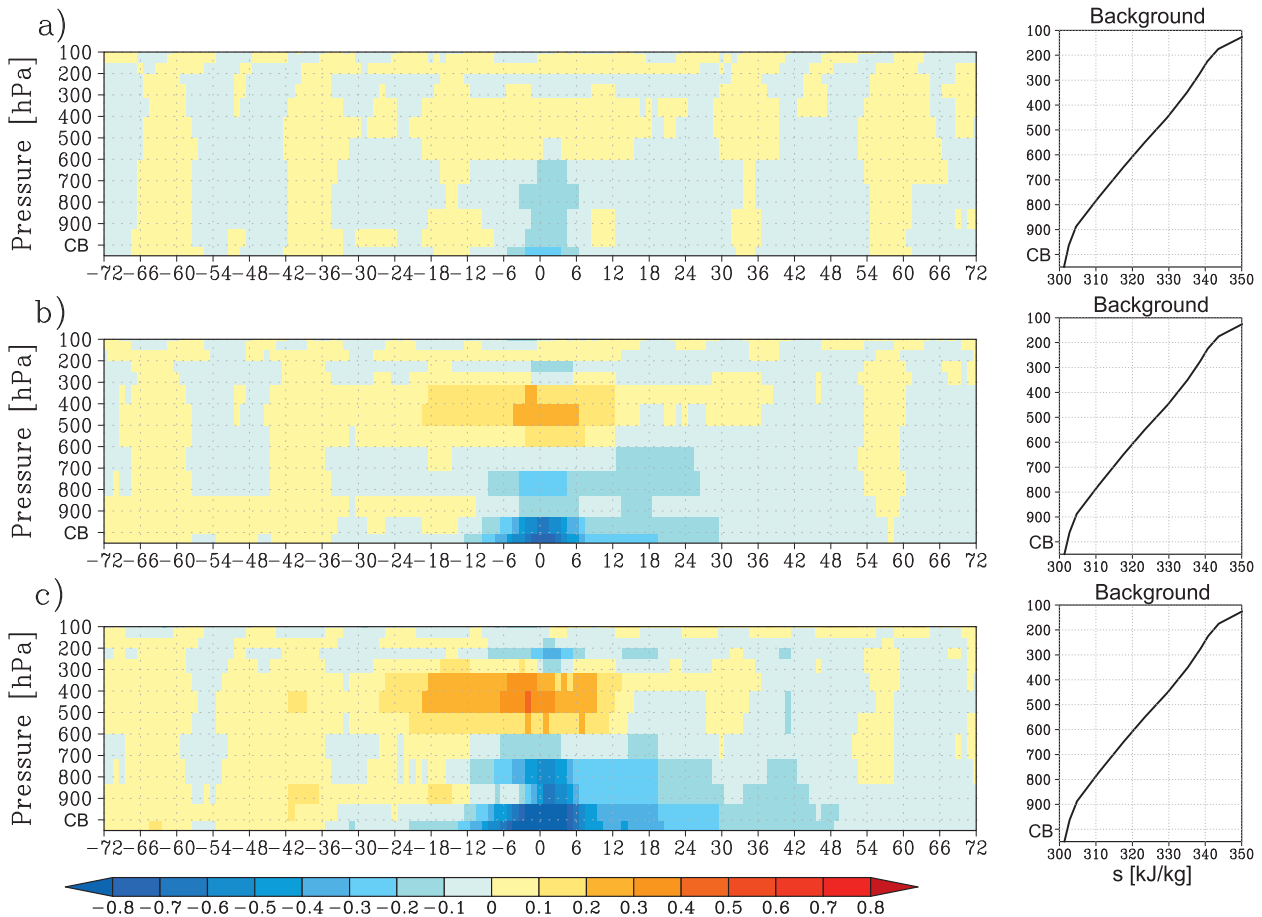


FIG. 4. As in Fig. 3, but for large-scale mean DSE \bar{s} (kJ kg^{-1}).

peaks (Sherwood and Wahrlich 1999; Mapes et al. 2006; Zelinka and Hartmann 2009; Masunaga 2012a). In particular, the very bottom layer exhibits a sudden drying immediately after time zero for highly organized systems.

Large-scale mean DSE per unit mass is

$$\bar{s}(p) = c_p \bar{T}(p) + \bar{\varphi}(p), \quad (10)$$

where c_p is the specific heat of dry air at constant pressure. As seen in Fig. 4, a negative DSE anomaly in the lower to middle troposphere emerges as convection develops in parallel with a positive anomaly growing in the upper troposphere. Such bipolar anomalies, only barely present for isolated cumuli, are robust for highly organized systems. A minor third pole of negative anomaly is also visible near the tropopause around $t = 0$. These characteristics are mainly attributed to the $c_p \bar{T}$ term. A similar dipole temperature anomaly has been observed in the past studies cited above with respect to the water vapor variability.

4. Budget analysis

The methodology and results of the water and heat budget analysis are presented in this section. Uncertainty estimates for the budget parameters are given in the appendix.

a. Tropospheric moisture and DSE convergences

The moisture and thermal budget equations are

$$\begin{aligned} \frac{\partial q}{\partial t} + \nabla \cdot q\mathbf{v} + \frac{\partial q\omega}{\partial p} &= e - c, \\ \frac{\partial s}{\partial t} + \nabla \cdot s\mathbf{v} + \frac{\partial s\omega}{\partial p} &= L(c - e) + Q_R, \end{aligned} \quad (11)$$

where \mathbf{v} is the horizontal velocity vector, ω is the vertical p velocity, e is the reevaporation rate per unit mass, c is the condensation rate per unit mass, L is the specific latent heat of liquid water, and Q_R is radiative heating rate per unit mass. Vertically integrating and horizontally averaging (11), one finds

$$\begin{aligned} \frac{\partial \overline{\langle q \rangle}}{\partial t} + \overline{\langle \mathbf{V} \cdot \mathbf{q} \mathbf{v} \rangle} &= \overline{E} - \overline{P}_s, \\ \frac{\partial \overline{\langle s \rangle}}{\partial t} + \overline{\langle \mathbf{V} \cdot \mathbf{s} \mathbf{v} \rangle} &= \overline{S} + L\overline{P}_s + \overline{\langle Q_R \rangle}, \end{aligned} \quad (12)$$

where E is the surface evaporation flux, P_s is the surface precipitation rate, S is the surface sensible heat flux, and angle brackets denote the vertical integral:

$$\langle \dots \rangle \equiv \int_{p_T}^{p_s} \dots \frac{dp}{g}, \quad (13)$$

where p_T is fixed at 100 hPa as a rough measure of the tropopause pressure. Here p_s and p_T are implicitly assumed to be independent of time, so the pressure integral and temporal derivative are interchangeable, that is, $\langle \partial/\partial t \dots \rangle = \partial/\partial t \langle \dots \rangle$. The surface turbulent fluxes are evaluated with the bulk formulas

$$\begin{aligned} E &= \rho_a C_E [q_{ss}^* - q(p_s)] |\mathbf{v}_{10}|, \\ S &= \rho_a C_\theta c_p [\theta_{ss} - \theta(p_s)] |\mathbf{v}_{10}|, \end{aligned} \quad (14)$$

where ρ_a , q_{ss}^* , θ , θ_{ss} , and \mathbf{v}_{10} are dry air density, saturation vapor mixing ratio for SST, potential temperature, sea surface potential temperature (which is numerically equivalent to SST), and wind vector at 10 m above the sea surface, respectively. The bulk transfer coefficients C_E and C_θ , adopted from Large et al. (1994), are

$$\begin{aligned} C_E &= 3.46 \times 10^{-2} \sqrt{C_D}, \\ C_\theta &= 3.27 \times 10^{-2} \sqrt{C_D}, \end{aligned}$$

where the drag coefficient C_D is given by

$$\begin{aligned} C_D &= 2.7 \times 10^{-3} \left[\frac{|\mathbf{v}_{10}|}{(\text{m s}^{-1})} \right]^{-1} + 1.42 \times 10^{-4} \\ &+ 7.64 \times 10^{-5} \left[\frac{|\mathbf{v}_{10}|}{(\text{m s}^{-1})} \right]. \end{aligned}$$

Observations yield the time series of \overline{E} and \overline{S} through (14) with observed \mathbf{v}_{10} as well as $\overline{\langle q \rangle}$, $\overline{\langle s \rangle}$, $\overline{\langle Q_R \rangle}$, and \overline{P}_s in composite space, where large-scale means are as given by (9) and pressure integrals are carried out numerically over discrete pressure levels. On the other hand, no satellite sensor currently available is capable to measure wind, and hence the convergence field, far above the surface. A solution to this problem is to employ the vertically integrated budget equations (12) for the diagnosis of moisture and DSE convergences, that is,

$$-\overline{\langle \mathbf{V} \cdot \mathbf{q} \mathbf{v} \rangle} = \frac{\partial \overline{\langle q \rangle}}{\partial t} - \overline{E} + \overline{P}_s \quad (15)$$

and

$$-\overline{\langle \mathbf{V} \cdot \mathbf{s} \mathbf{v} \rangle} = \frac{\partial \overline{\langle s \rangle}}{\partial t} - \overline{S} - L\overline{P}_s - \overline{\langle Q_R \rangle}. \quad (16)$$

Figure 5 shows the moisture budget breakdown. Evaporation E and precipitation P_s are roughly balanced against each other throughout when composited with respect to isolated cumulus clouds (Fig. 5a). Both E and P_s stay close to the background level of 0.2 mm h^{-1} , except for a slight enhancement in P_s near $t = 0$. Moisture convergence is comparable to E near its maximum but virtually absent during the rest of the period and only makes a modest contribution to the moisture budget. It follows that precipitation from isolated cumulus clouds does little more than consume the local moisture supply by evaporation from beneath. Precipitation in the background state itself is likely produced by isolated congestus clouds or precipitating shallow cumuli, which are ubiquitous across tropical oceans (Johnson et al. 1999; Short and Nakamura 2000).

In contrast, moisture convergence greatly strengthens as convection develops for more organized convective systems (Figs. 5b,c). Given that evaporation varies little beyond the background level in all cases, water vapor fed into intensifying rainfall must be accumulated dynamically through horizontal convergence. In particular, the moisture budget during highly organized systems virtually consists of a sole balance between precipitation and moisture convergence. As such, the nature of moisture budget associated with convective development qualitatively changes depending on the degree of convective organization.

The DSE budget is illustrated in Fig. 6. Isolated cumuli accompany little systematic variation in the DSE budget balance, where DSE divergence and column radiative cooling have a nearly equal amplitude of $\sim 0.1 \text{ kW m}^{-2}$ and together offset the net latent heating. Sensible heat flux stays negligibly small. In cases of more developed convection, DSE divergence and latent heating overwhelm Q_R and S and almost precisely counteract each other during active convection.

Typical values of the tropospheric budget parameters are comparable to in situ observations from past field campaigns. Some examples are given in the appendix.

b. FT moisture and DSE balance

The budget equations are further exploited to analyze the FT moisture and DSE budget. To facilitate this, the troposphere is divided into two layers separated by cloud base. The layers below and above cloud base define the subcloud layer (SC) and free troposphere, respectively, through the rest of the paper. The divergence terms are broken down into SC and FT components,

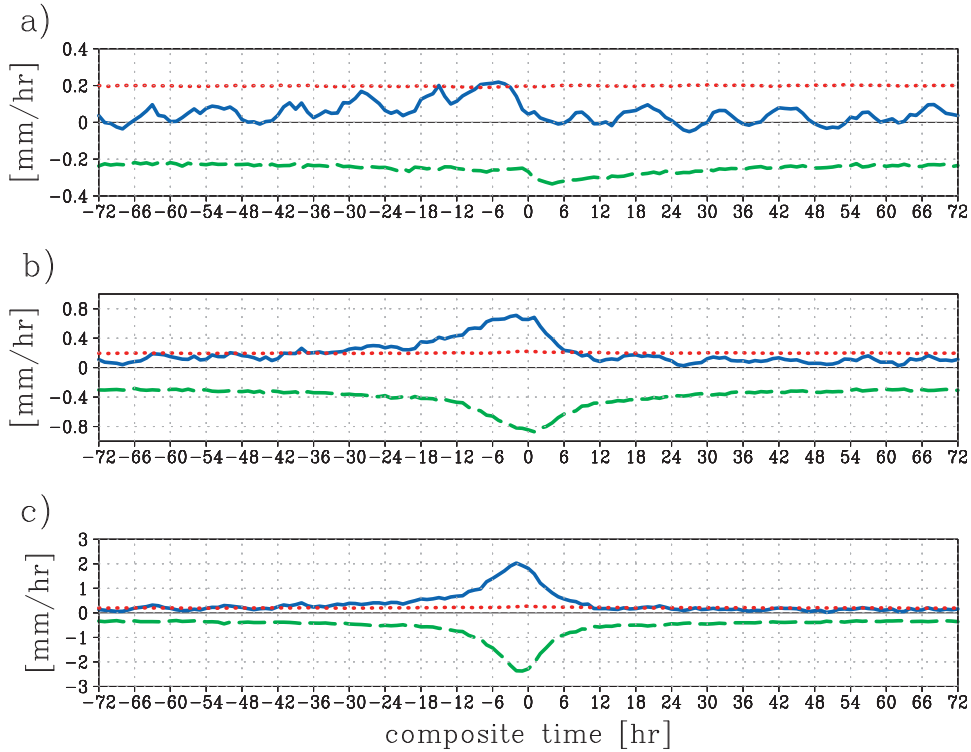


FIG. 5. The composite time series of large-scale mean moisture convergence $-\langle \nabla \cdot q \mathbf{v} \rangle$ (solid blue line), precipitation with sign reversed $-\bar{P}_s$ (dashed green line), and surface evaporation flux \bar{E} (dotted red line) (mm h^{-1}) for (a) isolated cumulus clouds, (b) moderately developed clouds, and (c) highly organized systems.

$$\begin{aligned} \overline{\langle \nabla \cdot q \mathbf{v} \rangle} &= \overline{\langle \nabla \cdot q \mathbf{v} \rangle}_{\text{FT}} + \overline{\langle \nabla \cdot q \mathbf{v} \rangle}_{\text{SC}}, \\ \overline{\langle \nabla \cdot s \mathbf{v} \rangle} &= \overline{\langle \nabla \cdot s \mathbf{v} \rangle}_{\text{FT}} + \overline{\langle \nabla \cdot s \mathbf{v} \rangle}_{\text{SC}}, \end{aligned} \quad (17)$$

where

$$\begin{aligned} \langle \cdots \rangle_{\text{FT}} &\equiv \int_{p_T}^{p_{\text{CB}}} \cdots \frac{dp}{g}, \\ \langle \cdots \rangle_{\text{SC}} &\equiv \int_{p_{\text{CB}}}^{p_s} \cdots \frac{dp}{g}. \end{aligned}$$

The subcloud layer is assumed to be well mixed over height dynamically and thermodynamically at any moment, so that q , s , and \mathbf{v}_{10} are each vertically homogeneous below cloud base. The SC divergence terms are then explicitly expressed in terms of observed $q(p_s)$, $s(p_s)$, and \mathbf{v}_{10} as

$$\begin{aligned} \overline{\langle \nabla \cdot q \mathbf{v} \rangle}_{\text{SC}} &= \overline{\nabla \cdot [q(p_s) \mathbf{v}_{10}] \frac{\Delta p_{\text{SC}}}{g}}, \\ \overline{\langle \nabla \cdot s \mathbf{v} \rangle}_{\text{SC}} &= \overline{\nabla \cdot [s(p_s) \mathbf{v}_{10}] \frac{\Delta p_{\text{SC}}}{g}}, \end{aligned} \quad (18)$$

where $\Delta p_{\text{SC}} \equiv p_s - p_{\text{CB}}$. The SC divergence turns out to consist of known quantities only and is differentiated for numerical integration as

$$\begin{aligned} \nabla \cdot [q(p_s) \mathbf{v}_{10}] \frac{\Delta p_{\text{SC}}}{g} \Big|_{i-(1/2)} &= 2 \left\{ \frac{[rq(p_s)u_{10}]_i - [rq(p_s)u_{10}]_{i-1}}{r_i^2 - r_{i-1}^2} \right\} \left(\frac{\Delta p_{\text{SC}}}{g} \right)_{i-(1/2)}, \\ \nabla \cdot [s(p_s) \mathbf{v}_{10}] \frac{\Delta p_{\text{SC}}}{g} \Big|_{i-(1/2)} &= 2 \left\{ \frac{[rs(p_s)u_{10}]_i - [rs(p_s)u_{10}]_{i-1}}{r_i^2 - r_{i-1}^2} \right\} \left(\frac{\Delta p_{\text{SC}}}{g} \right)_{i-(1/2)}. \end{aligned}$$

Large-scale mean SC divergence (18) is rewritten with the help of (9) into

$$\begin{aligned} \overline{\nabla \cdot [q(p_s) \mathbf{v}_{10}] \frac{\Delta p_{\text{SC}}}{g}} &= \frac{2}{R^2} \sum_{i=1}^N \{ [rq(p_s)u_{10}]_i - [rq(p_s)u_{10}]_{i-1} \} \left(\frac{\Delta p_{\text{SC}}}{g} \right)_{i-(1/2)}, \\ \overline{\nabla \cdot [s(p_s) \mathbf{v}_{10}] \frac{\Delta p_{\text{SC}}}{g}} &= \frac{2}{R^2} \sum_{i=1}^N \{ [rs(p_s)u_{10}]_i - [rs(p_s)u_{10}]_{i-1} \} \left(\frac{\Delta p_{\text{SC}}}{g} \right)_{i-(1/2)}, \end{aligned} \quad (19)$$

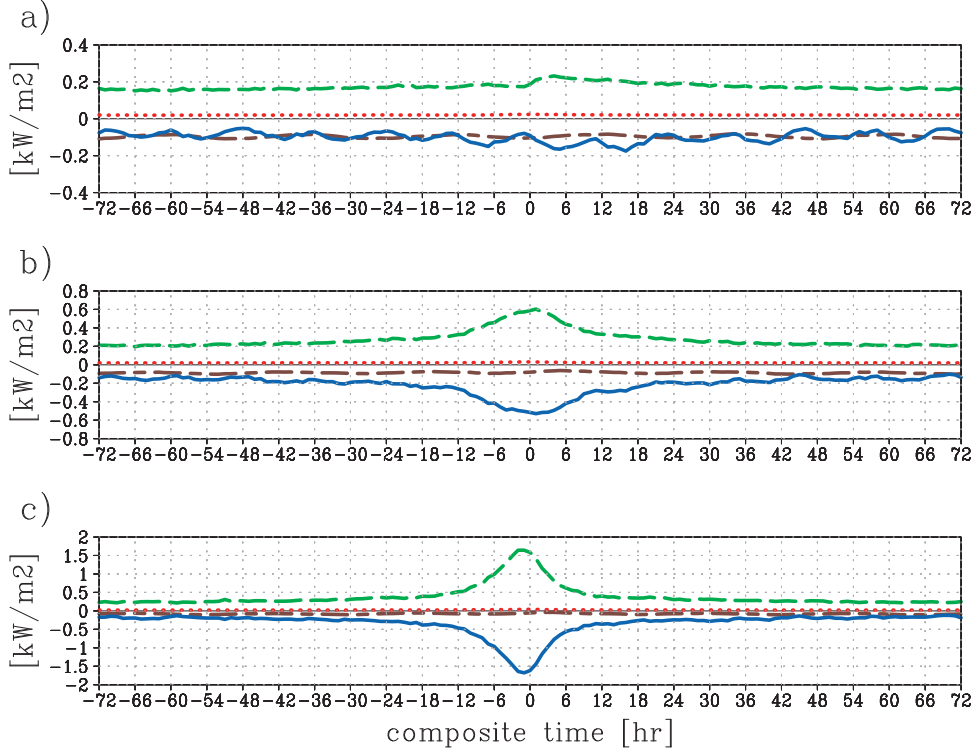


FIG. 6. As in Fig. 5, but for DSE convergence $-\langle \mathbf{V} \cdot s\mathbf{v} \rangle$ (solid blue line), net latent heating $L\bar{P}_s$ (dashed green line), sensible heat flux \bar{S} (dotted red line), and column radiative heating $\langle Q_R \rangle$ (dot-dashed brown line).

where u_{10} is the radial component of \mathbf{v}_{10} . The summation would collapse to the boundary ($i = N$) term in the divergence theorem, but all terms must be retained in our case. Those terms are not precisely, though mostly, cancelled out because Δp_{SC} changes with r depending on $q(p_s)$ and $T(p_s)$. Equations (12), (17), and (18) lead to

$$-\langle \mathbf{V} \cdot q\mathbf{v} \rangle_{FT} = \frac{\partial}{\partial t} \langle q \rangle + \nabla \cdot [q(p_s)\mathbf{v}_{10}] \frac{\Delta p_{SC}}{g} - \bar{E} + \bar{P}_s \quad (20)$$

and

$$-\langle \mathbf{V} \cdot s\mathbf{v} \rangle_{FT} = \frac{\partial}{\partial t} \langle s \rangle + \nabla \cdot [s(p_s)\mathbf{v}_{10}] \frac{\Delta p_{SC}}{g} - \bar{S} - L\bar{P}_s - \langle Q_R \rangle, \quad (21)$$

which offer an observational diagnosis of FT convergence.

The large-scale SC budget equations, obtained by integrating (11) over the subcloud layer and applying domain average, are

$$\begin{aligned} \left\langle \frac{\partial q}{\partial t} \right\rangle_{SC} + \langle \mathbf{V} \cdot q\mathbf{v} \rangle_{SC} - \left. \frac{q\bar{\omega}}{g} \right|_{CB} &= \bar{E} + \bar{P}_{CB} - \bar{P}_s, \\ \left\langle \frac{\partial s}{\partial t} \right\rangle_{SC} + \langle \mathbf{V} \cdot s\mathbf{v} \rangle_{SC} - \left. \frac{s\bar{\omega}}{g} \right|_{CB} &= \bar{S} + L(\bar{P}_s - \bar{P}_{CB}) \\ &\quad + \langle Q_R \rangle_{SC}, \end{aligned} \quad (22)$$

where P_{CB} is the rate of precipitation entering the subcloud layer from above through cloud base. The tendency terms integrated over a well-mixed subcloud layer are

$$\begin{aligned} \left\langle \frac{\partial q}{\partial t} \right\rangle_{SC} &= \frac{\partial q(p_s)}{\partial t} \frac{\Delta p_{SC}}{g}, \\ \left\langle \frac{\partial s}{\partial t} \right\rangle_{SC} &= \frac{\partial s(p_s)}{\partial t} \frac{\Delta p_{SC}}{g}. \end{aligned} \quad (23)$$

The term $P_{CB} - P_s$ in (22) accounts for the moistening and cooling due to reevaporation from raindrops within the subcloud layer. Since the SC reevaporation is very difficult to observationally constrain, the effects of reevaporation are characterized by a prescribed coefficient α_{SC} , defined as the SC reevaporation rate normalized by surface rain rate:

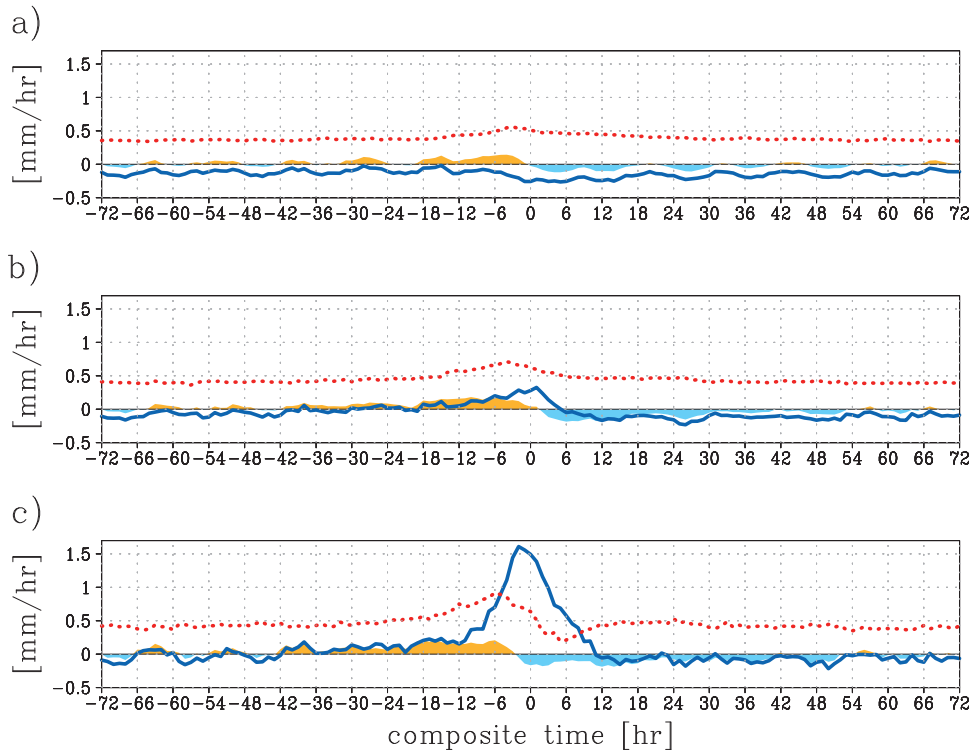


FIG. 7. As in Fig. 5, but for FT moisture convergence $-\overline{(\mathbf{V} \cdot q\mathbf{v})}_{\text{FT}}$ (solid blue line), vertical moisture flux at cloud base $-\overline{q\omega}/g|_{\text{CB}}$ (dotted red line), and FT-integrated water vapor tendency $\overline{(\partial q/\partial t)}_{\text{FT}}$ (shaded in yellow where positive and in light blue where negative).

$$P_{\text{CB}} - P_s \equiv \alpha_{\text{SC}} P_s. \quad (24)$$

Throughout this section α_{SC} is fixed at zero, that is, all rainwater falling into the subcloud layer is assumed to precipitate out to the surface without being evaporated at all. This assumption is not fully valid, and the potential impacts of a nonzero α_{SC} will be discussed in section 5d.

Equations to evaluate the vertical transport (defined positive upward) are derived from (18), (22), (23), and (24) as

$$-\left. \frac{\overline{q\omega}}{g} \right|_{\text{CB}} = -\frac{\overline{\partial q(p_s) \Delta p_{\text{SC}}}}{\partial t} \frac{\Delta p_{\text{SC}}}{g} - \overline{\mathbf{V} \cdot [q(p_s) \mathbf{v}_{10}]} \frac{\Delta p_{\text{SC}}}{g} + \overline{E} + \alpha_{\text{SC}} \overline{P}_s \quad (25)$$

for moisture and

$$-\left. \frac{\overline{s\omega}}{g} \right|_{\text{CB}} = -\frac{\overline{\partial s(p_s) \Delta p_{\text{SC}}}}{\partial t} \frac{\Delta p_{\text{SC}}}{g} - \overline{\mathbf{V} \cdot [s(p_s) \mathbf{v}_{10}]} \frac{\Delta p_{\text{SC}}}{g} + \overline{S} - \alpha_{\text{SC}} \overline{L P}_s + \overline{Q_R}_{\text{SC}} \quad (26)$$

for DSE.

FT moisture convergence and vertical moisture transport at cloud base are now ready to be individually evaluated with (20) and (25). These two quantities are the origins of FT moistening during convection as seen in the FT-integrated moisture budget,

$$\overline{\left\langle \frac{\partial q}{\partial t} \right\rangle}_{\text{FT}} = -\overline{(\mathbf{V} \cdot q\mathbf{v})}_{\text{FT}} - \left. \frac{\overline{q\omega}}{g} \right|_{\text{CB}} - \overline{P}_{\text{CB}}. \quad (27)$$

The result for isolated cumuli (Fig. 7a) shows that the free troposphere is constantly exposed to a vertical moisture flux of $\sim 0.5 \text{ mm h}^{-1}$ through cloud base (red), while horizontal moisture flow remains weakly diverging (blue). Horizontal moisture convergence changes its sign to positive momentarily for moderately developed clouds but is still consistently weak (Fig. 7b). The primary source of the FT moistening associated with these clouds is hence the moist SC air beneath without much help from lateral convergence. When highly organized systems occur (Fig. 7c), FT moisture convergence largely exceeds vertical moisture transport during $\pm 6 \text{ h}$ around the convective peak. FT convergence sharply rises toward its peak slightly before time zero, while vertical transport reaches a modest peak at -6 h and then drops until it hits the minimum at $+6 \text{ h}$.

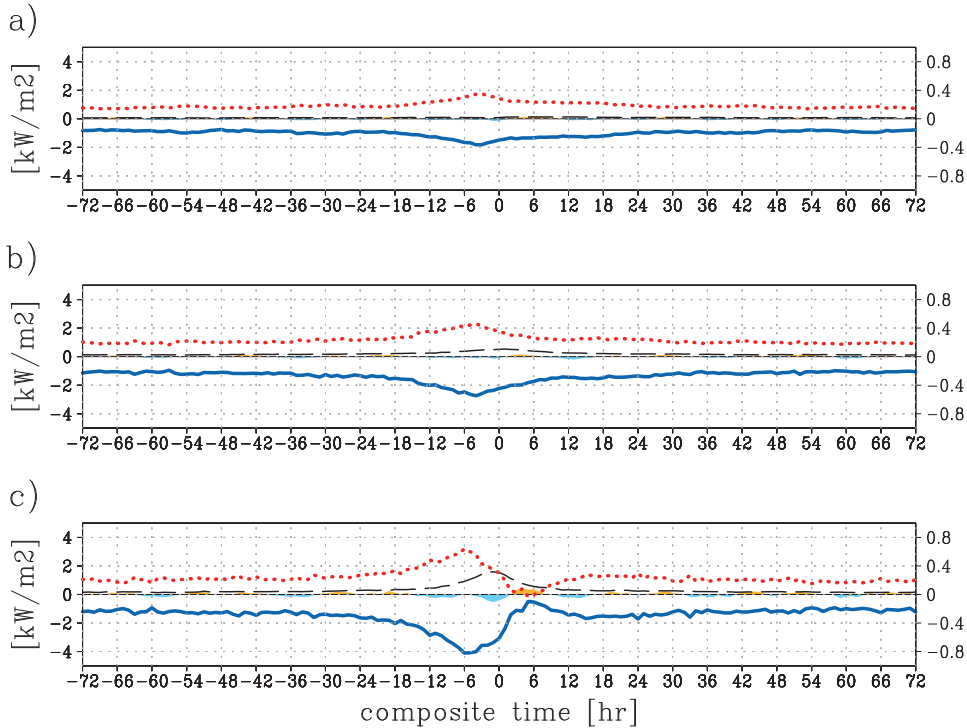


FIG. 8. As in Fig. 7, but for FT DSE convergence $-\langle \mathbf{V} \cdot \mathbf{s}\mathbf{v} \rangle_{\text{FT}}$ (solid blue line, labeled on left), vertical DSE flux at cloud base $-\overline{s\omega}|_{\text{CB}}$ (dotted red line, labeled on left), FT diabatic heating $L\overline{P}_s + \langle Q_R \rangle_{\text{FT}}$ (dashed black line, labeled on left), and FT-integrated DSE tendency $\langle \partial s / \partial t \rangle_{\text{FT}}$ (shaded, labeled on right).

The tendency of FT-integrated water vapor $\langle \partial q / \partial t \rangle_{\text{FT}}$ (shaded in Fig. 7) is positive until convection peaks and then suddenly jumps down to negative, although persistently weak in magnitude compared to the dominant moisture sources discussed above. It is implied from (27) that an FT moisture accumulation due to lateral convergence and vertical transport should to a large degree precipitate out instantly, whereas a measurable amount of moisture residual (deficit) is left behind before (after) the time of peak convection. The moisture storage is about $\pm 0.1 \text{ mm h}^{-1}$ over an extended period of time, barely standing out above moisture budget uncertainties (see the appendix). The FT moistening before convection and drying after are visually evident in the vertical vapor structure, as we have seen in Fig. 3.

Figure 8 shows the FT DSE budget, where horizontal convergence and vertical transport at cloud base look as if they were mirrored to each other. The two curves have a comparable amplitude, but a close examination reveals that DSE is laterally diverged out of the free troposphere somewhat more than input from the subcloud layer during the convectively active phase. The DSE tendency is considerably small in magnitude relative to other budget parameters (note that the tendency plot is

vertically stretched by 5 times and labeled on the right). Net latent heating and radiative cooling, plotted together in the dashed curve, therefore virtually offset the deficit in the total (horizontal plus vertical) DSE convergence, as inferred from the FT DSE budget balance,

$$\left\langle \frac{\partial s}{\partial t} \right\rangle_{\text{FT}} = -\langle \mathbf{V} \cdot \mathbf{s}\mathbf{v} \rangle_{\text{FT}} - \left. \frac{s\overline{\omega}}{g} \right|_{\text{CB}} + L\overline{P}_{\text{CB}} + \langle Q_R \rangle_{\text{FT}}. \quad (28)$$

No attempt has been made so far to break down the vertical moisture or DSE transport into large-scale and eddy components. The effects of large-scale mean updraft and convective eddies are separately examined next.

c. Vertical eddy transport at cloud base

Vertical eddy transport at cloud base can be diagnosed by the remainder after subtracting the large-scale term (vertical flux due to large-scale mean updraft or downdraft) from the net vertical transport derived in the previous section,

$$\begin{aligned} -\frac{\overline{q'\omega'}}{g}\Big|_{\text{CB}} &= -\frac{\overline{q\omega}}{g}\Big|_{\text{CB}} + \frac{\overline{q}_{\text{CB}}\overline{\omega}_{\text{CB}}}{g}, \\ -\frac{\overline{s'\omega'}}{g}\Big|_{\text{CB}} &= -\frac{\overline{s\omega}}{g}\Big|_{\text{CB}} + \frac{\overline{s}_{\text{CB}}\overline{\omega}_{\text{CB}}}{g}. \end{aligned} \quad (29)$$

The last term is explicitly computed from individual large-scale mean parameters. Large-scale mean vertical velocity at cloud base is computed from the incompressible continuity equation,

$$\overline{\omega}_{\text{CB}} = \overline{\omega}(p_s) - \int_{p_s}^{p_{\text{CB}}} \overline{\nabla \cdot \mathbf{v}} dp, \quad (30)$$

where $\overline{\omega}(p_s)$ is practically negligible and will be omitted hereafter. Recalling the assumption that the subcloud layer is well mixed, (30) is simplified similarly to (18) and (19) into

$$\begin{aligned} \overline{\omega}_{\text{CB}} &= \overline{(\nabla \cdot \mathbf{v}_{10})\Delta p_{\text{SC}}} \\ &= \frac{2}{R^2} \sum_{i=1}^N [(ru_{10})_i - (ru_{10})_{i-1}](\Delta p_{\text{SC}})_{i-(1/2)}. \end{aligned} \quad (31)$$

Large-scale mean vapor mixing ratio and DSE at cloud base are chosen to be “upwind” depending on the sign of $\overline{\omega}_{\text{CB}}$: \overline{q}_{CB} and \overline{s}_{CB} are replaced by the SC values, $\overline{q}(p_s)$ and $\overline{s}(p_s)$, in case of updraft ($\overline{\omega}_{\text{CB}} < 0$), while otherwise observations from the layer immediately above cloud base are adopted. Vertical eddy transport is evaluated with (25), (26), and (31) substituted for the right-hand side of (29).

As shown in Fig. 9, the large-scale and eddy components of vertical moisture transport are comparable in magnitude to each other in the background state. Eddy flux does not much deviate from the background level even for highly organized systems, while large-scale mean updraft is significantly modulated during convection. Large-scale mean updraft hits a minimum of near zero at +6 h for highly organized systems, presumably signifying a mesoscale downdraft (Zipser 1969, 1977) just as strong as entirely cancels large-scale mean updraft. The tendency of SC vapor mixing ratio stays minimal throughout, except for a momentary negative (SC ventilation by convection), barely recognizable around the peak of organized convection. Figure 10 illustrates the vertical DSE transport terms, where large-scale mean updraft (labeled on right) is larger by an order of magnitude or two than the eddy contribution (labeled on left), regardless of the degree of convective organization. The SC DSE tendency is overall small, except for several hours after time zero, during which the DSE

tendency is not necessarily negligible compared to the other terms.

5. Discussion

In this section, the present results are discussed in light of the implications for related research topics.

a. Subcloud-layer budget

1) ORIGINS OF SC COOLING DURING CONVECTION

Figure 4 shows that the lower troposphere, including the subcloud layer, experiences a temporary cool anomaly during convection. The plausible sources of the cool anomaly include rain reevaporation and large-scale ascent, although they each have a difficulty in thoroughly explaining the SC cooling as observed. The SC cool anomaly strengthens toward $t = 0$ and then gradually weakens (Fig. 4), indicating a cooling before time zero and a heating after. This is, however, contrary to what one might expect from rain reevaporation. Lower-tropospheric evaporative cooling is characteristic of stratiform precipitation, which is known to be most dominant at later stages in the life cycle of organized convective systems. Figure 4c shows that the lower-tropospheric cool anomaly for highly organized systems continues to grow even during the peak rainfall (slightly earlier than time zero, as observed in Fig. 5c), which is likely brought primarily by deep convective precipitation. On the other hand, the observed DSE profile does not appear to support the adiabatic cooling hypothesis either. Updraft velocity is generally greatest in the midtroposphere, and the static stability is weakest near the surface, as seen from the background DSE profile in Fig. 4. Neither of these facts favors the presence of a cooling peak near the bottom of the atmosphere, as observed in Fig. 4.

Evaporative and adiabatic coolings are thus unlikely capable to individually account for the SC cooling, although both in tandem might be able to better explain it. Unfortunately, it is difficult in any case to isolate the origins of SC cooling from the thermal budget perspective because the DSE storage term is minimal throughout the evolution (Fig. 10). The SC DSE tendency in Fig. 4 shows an approximately 1 kJ kg^{-1} decrease over 12 h, resulting in a cooling as small as $10^{-2} \text{ kW m}^{-2}$ for an SC thickness of 50 hPa. The SC budget terms stay well balanced nearly all the time, suggesting a mechanism that instantly removes an excessive SC moisture and DSE through convective updraft and associated downdraft (Raymond 1995; Emanuel 1995).

In contrast to its minimum consequences for the thermal budget, SC cooling (along with moistening)

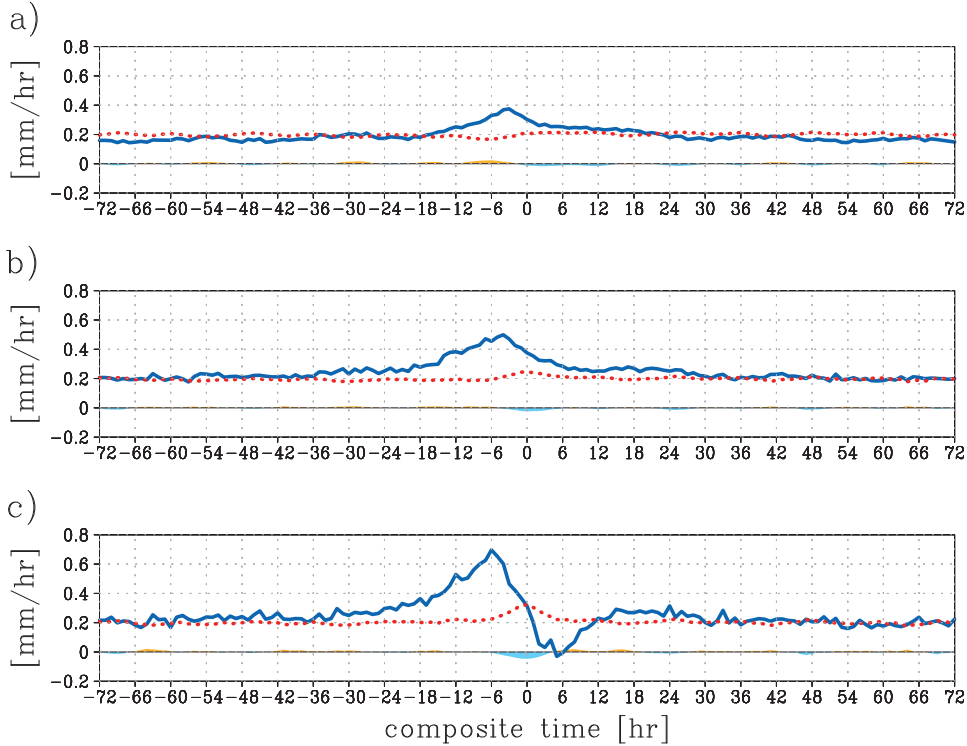


FIG. 9. As in Fig. 7, but for vertical moisture transport at cloud base due to large-scale motions $-\bar{q}_{CB}\bar{\omega}_{CB}/g$ (solid blue line) and due to convective-scale eddies $-\bar{q}'\omega'/g|_{CB}$ (dotted red line) and the SC moisture tendency $\langle\partial q/\partial t\rangle_{SC}$ (shaded).

leads to a significant modulation of cloud-base height, which could be a key factor governing the convective onset and intensity. This is examined next.

2) MODULATION OF SC THICKNESS

Cloud-base pressure experiences a systematic temporal variation in the course of convective development. Figure 11a shows that cloud base decreases in height as convection intensifies and then increases back after convection ceases, with a greater magnitude for organized convective systems than for isolated cumuli. Cloud-base pressure rises from 955 to 975 hPa toward the convective peak for highly organized systems. Fluctuations in cloud-base height, by definition of LCL, result from temperature and water vapor perturbations near the surface. A slight but consistent SC moistening for hours prior to convection (Fig. 11c) explains the initial, gradual decrease of cloud-base height. An SC temperature drop immediately before the convective peak (Fig. 11d) leads to an increase of SC relative humidity and, as a result, further lowers the cloud base, while a subsequent temperature recovery appears to rapidly raise cloud-base height back toward the initial level. In contrast to p_{CB} , surface pressure stays virtually invariable during the whole period of time analyzed

(Fig. 11b), letting cloud base be solely responsible for the variability of SC thickness.

A thinning of the subcloud layer would reduce convective inhibition and potentially facilitate the onset of convection. On the other hand, Masunaga (2012a) found that the SC cooling results in a remarkable decrease of convective available potential energy (CAPE), and the troposphere does not as a whole stay in a quasi-equilibrium state. These behaviors appear to favor the “activation control” hypothesis for the large-scale variability of deep convection (Mapes 1997).

3) SCALE ANALYSIS

A scale analysis is carried out here for the SC budget in order to provide an intuitive interpretation of the eddy moisture and DSE transports at cloud base. The large-scale mean moisture convergence may be approximated in the integral form [see note following (19)] as

$$\overline{\langle \mathbf{V} \cdot q \mathbf{v} \rangle}_{SC} = \frac{1}{A} \int_{p_{CB}}^{p_s} \frac{dp}{g} \oint q u dl, \quad (32)$$

where A designates the large-scale domain area, the line integral over dl applies to the domain border, and u is

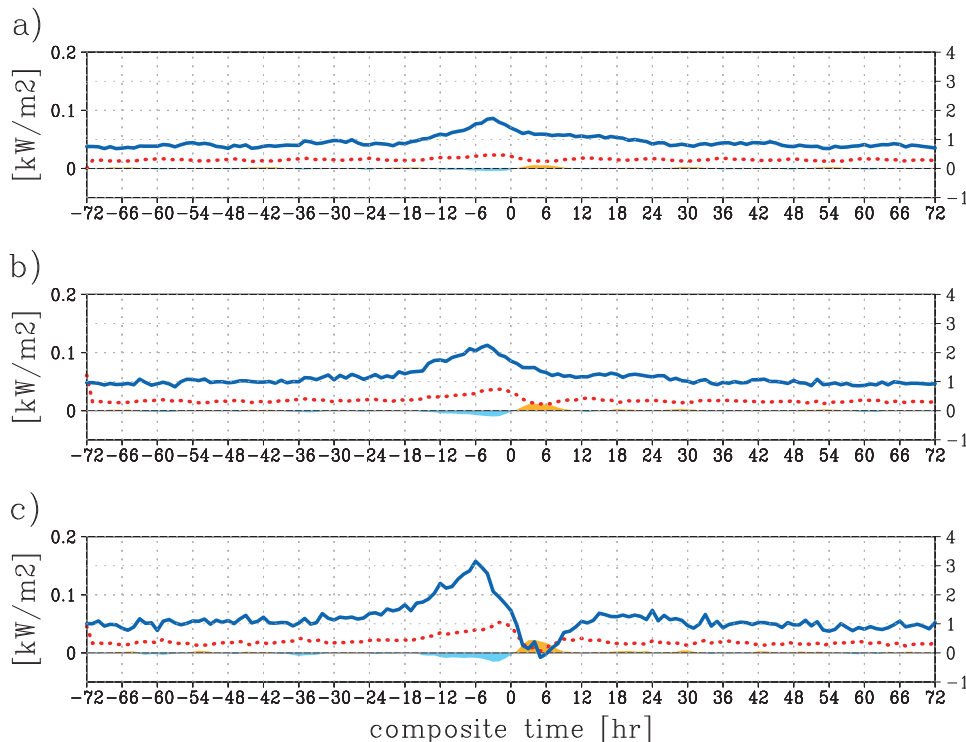


FIG. 10. As in Fig. 9, but for vertical DSE transport at cloud base due to large-scale motions $-\bar{s}_{\text{CB}}\bar{\omega}_{\text{CB}}/g$ (solid blue line, labeled on right) and due to convective-scale eddies $-s'\omega'/g|_{\text{CB}}$ (dotted red line, labeled on left) and SC DSE tendency $\langle \partial s / \partial t \rangle_{\text{SC}}$ (shaded, labeled on left).

the normal component of horizontal wind on the border (outward positive). The mass conservation over the large-scale domain (30) is rewritten similarly as

$$\bar{\omega}_{\text{CB}} = \frac{1}{A} \int_{p_{\text{CB}}}^{p_s} dp \oint u dl.$$

Since it can be safely assumed for a scale analysis that SC vapor mixing ratio is nearly uniform throughout the large-scale domain of interest, q can be moved out of the integral in (32) as

$$\overline{\langle \mathbf{V} \cdot q\mathbf{V} \rangle}_{\text{SC}} \approx \frac{1}{A} \bar{q}_{\text{CB}} \int_{p_{\text{CB}}}^{p_s} \frac{dp}{g} \oint u dl = \frac{\bar{q}_{\text{CB}} \bar{\omega}_{\text{CB}}}{g}, \quad (33)$$

where SC vapor mixing ratio, being constant across height, has been replaced by the value at its upper end, \bar{q}_{CB} , for later convenience. A parallel argument applies to the DSE budget as well, and

$$\overline{\langle \mathbf{V} \cdot s\mathbf{V} \rangle}_{\text{SC}} \approx \frac{\bar{s}_{\text{CB}} \bar{\omega}_{\text{CB}}}{g}. \quad (34)$$

Inserting (24), (29), (33), and (34) into the SC budget equation (22), one obtains

$$-\left. \frac{\bar{q}'\omega'}{g} \right|_{\text{CB}} \approx \bar{E} + \alpha_{\text{SC}} \bar{P}_s \quad (35)$$

and

$$-\left. \frac{s'\omega'}{g} \right|_{\text{CB}} \approx \bar{S} - \alpha_{\text{SC}} L \bar{P}_s + \overline{\langle Q_R \rangle}_{\text{SC}}. \quad (36)$$

We have assumed that the moisture and DSE tendencies are practically negligible, as we have seen earlier. Equations (35) and (36) state that vertical eddy transport at cloud base adjusts itself to balance with surface turbulent fluxes and reevaporation (and radiative cooling) within the subcloud layer, while SC horizontal convergence is largely compensated by large-scale mean updraft through cloud base [(33) and (34)]. In other words, large-scale dynamics hardly involves a net change in the SC budget, leaving surface forcing and diabatic sources alone to be counteracted by vertical eddy flux at cloud base. The vertical eddy flux of SC moisture is expected from (35) to simply equate with evaporation from below when α_{SC} is negligibly small. One can see that moisture eddy transport (Fig. 9) is indeed in close accordance with surface evaporation flux in Fig. 5.

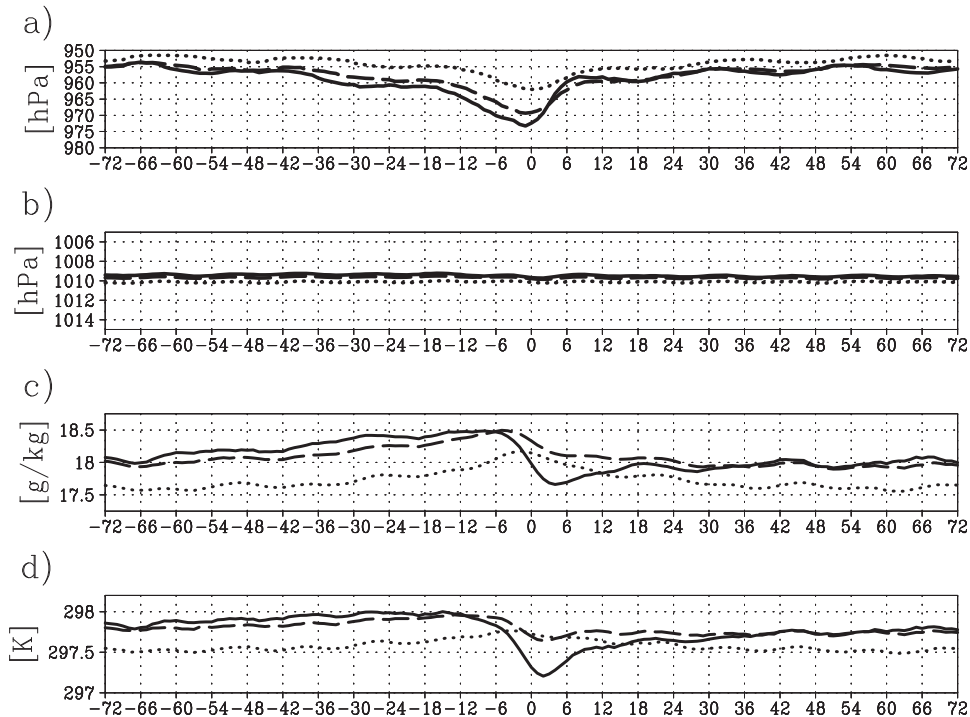


FIG. 11. The composite time series of large-scale mean (a) cloud-base pressure p_{CB} (hPa), (b) surface pressure p_s (hPa), (c) SC vapor mixing ratio (kg kg^{-1}), and (d) SC air temperature (K) for isolated cumulus clouds (dotted), moderately developed clouds (dashed), and highly organized systems (solid).

Similarly, (36) implies that DSE eddy transport at cloud base would compensate for sensible heat flux and SC-integrated radiative cooling, which, however, make little contribution to the DSE budget in the first place. As a result, vertical DSE eddy flux stays considerably small compared to large-scale mean updraft, as seen earlier in Fig. 10. It is noted that although vertical eddy flux at cloud base is minimal across tropical oceans, DSE eddy flux would play a critical role for afternoon storms over land where surface sensible heat flux is a dominant factor in the thermal budget.

b. FT budget

1) CONGESTUS MOISTENING

An FT moistening prior to convection is clearly observed in the present analysis in line with many existing studies reviewed in section 1. It was found that eddy moisture flux by background congestus clouds, composed of nearly equal shares of eddy and large-scale contributions, balances approximately with surface evaporation, as shown by (35). Evaporation, in turn, is largely offset by precipitation from isolated cumuli themselves (Fig. 5a). This equilibrium between eddy moisture flux and congestus precipitation accounts for the moisture balance in the background state being away

from the times of organized convection. After a long spell with no systematic trend in the background state, a small but consistent FT moistening begins (shading in Fig. 7c) and convective clouds start to deepen (Fig. 2c) around 30 h before highly organized systems reach the peak. Beyond this point, large-scale mean updraft strengthens while eddy moisture flux remains hardly changed (Fig. 9c), and then horizontal moisture convergence takes the lead of FT moistening within a half day before the peak of highly organized systems (Fig. 7c). FT moistening within a few days before peak convection is therefore explained principally by large-scale mean updraft, with the effect of convective eddies being secondary.

Hohenegger and Stevens (2013) showed that congestus clouds moisten the free troposphere too slowly to explain the fast transition to deep convection as observed, while large-scale ascent provides a more efficient mechanism of FT moistening. Their conclusion, although obtained from a quite different approach from the present analysis, corroborates the current findings. The known relationship of FT moistening with congestus clouds (see section 1 for references) is probably an indirect correlation via large-scale vertical motion associated with deep convective development, so that the causal link between the congestus eddy moistening

and subsequent deep convection is weak on daily and hourly time scales. This point was not addressed by Kuang and Bretherton (2006) and Waite and Khouider (2010), who did not impose a large-scale vertical motion in their model simulations.

It should be noted, however, that observed large-scale mean updraft includes not only external dynamics such as synoptic-scale waves but the local effect of convective updraft unless convective updraft is largely cancelled out by environmental subsidence. It is very difficult to track down in observations to what extent the $\overline{q}_{CB}\overline{\omega}_{CB}$ term in (29) is driven by an external large-scale forcing or a local congestus-induced effect. It would be safe to conclude that congestus *eddy* moistening is unlikely a chief mechanism for preconditioning deep convective development, while congestus clouds could help moisten the free troposphere to some degree through their own updraft that survives large-scale averaging. Furthermore, the possibility is not ruled out that congestus moistening could be more important on a much longer time scale (e.g., MJO) than currently considered.

2) OTHER IMPLICATIONS

FT moisture is weakly diverging in the absence of vigorous convection growing beyond isolated cumuli (Fig. 7a) and turns to converging only when convection is developed into a more or less organized system (Figs. 7b,c). DSE diverges out of the free troposphere all the time and, contrary to FT moisture, becomes even more diverging during organized convection (Fig. 8). The weak FT divergence for isolated cumuli is explained by a modest updraft from the subcloud layer associated with shallow, sporadic convection that diverges out immediately above cloud base. Once convection becomes deep and organized, the lower free troposphere should be now converging in phase with the subcloud layer and accompany a significant upper-tropospheric divergence that exports updraft air from beneath. Such an overturning circulation with a lower inflow and a upper outflow would give rise to a moisture convergence and a DSE divergence as observed, given that water vapor mixing ratio decreases with height while DSE increases (see background fields in Figs. 3 and 4).

The FT DSE divergence and vertical DSE transport through cloud base are together largely cancelled out by domain-averaged diabatic heating on an instantaneous basis. This is as expected since an FT temperature perturbation would quickly dissipate out by gravity waves in the tropics. Nevertheless, a small but finite DSE imbalance is left behind, giving rise to a well-defined bipolar pattern containing a lower-tropospheric negative anomaly and an upper-tropospheric positive anomaly (Fig. 4). This feature implies that the troposphere is

temporarily stabilized to some extent in the course of the deep convective development (Masunaga 2012a). Possible mechanisms relating convection and stability over a time scale of present interest include the “diurnal dancing” hypothesis proposed by Chen and Houze (1997). Raymond and Sessions (2007) discussed a potential mechanism where such a stable perturbation favors the convective intensification in the context of tropical cyclogenesis.

The causes for the FT warming and cooling anomalies are difficult to identify, just as was the case for the SC budget discussed in section 5a(1). An FT DSE perturbation could be due partly to local diabatic heating and/or large-scale adiabatic cooling. The full vertical structure of atmospheric heating rate is not available in the current two-layer model approach and should be studied elsewhere so as to track down the origins of thermal budget imbalances in the free troposphere.

c. Regional variability

The composite plots presented so far represent the global tropical ocean as a whole, although the moisture and thermal budget characteristics may vary from region to region. This section is devoted to a brief assessment of the regional variability with focus on four major oceanic basins: Indian (50° – 90° E), western Pacific (140° E– 180°), eastern Pacific (130° – 90° W), and Atlantic (50° – 10° W) Oceans. All of the regions are meridionally bound between 15° N and 15° S, with landmasses excluded.

Figure 12a shows composite FT moisture convergence and vertical moisture flux at cloud base for highly organized systems (cf. Fig. 7c). The isolated cumulus and moderately developed cloud categories are omitted because well-developed convective systems are more clearly linked to the regionality than shallower clouds (e.g., Masunaga and Kummerow 2006). The regional breakdown makes the composite curves somewhat noisy as a result of the reduction of sample size compared to the global statistics. Besides the statistical fluctuations, no apparent regional difference is observed in the moisture budget characteristics. The qualitative behavior is similar across all regions also in the thermal budget properties (Fig. 12b), except that the eastern Pacific appears to have a slightly larger amplitude than other regions in both FT DSE convergence and vertical DSE flux at cloud base.

The DSE budget directly reflects the dynamic environment as implied by Fig. 12c. SC wind convergence, $-\langle \nabla \cdot \mathbf{v} \rangle_{SC}$, stays strongest, marginally but consistently over time, in the eastern Pacific, presumably related to a well-defined band of the intertropical convergence zone (ITCZ) unique to this region. Precipitation, meanwhile, is far less regionally sensitive (Fig. 12d), assuring that the

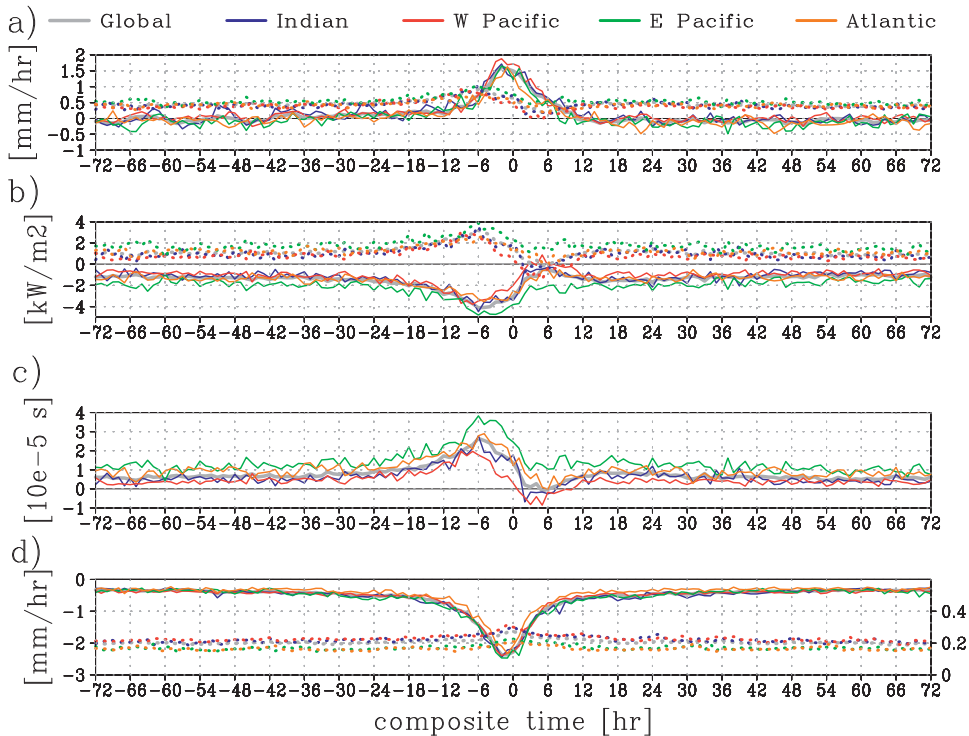


FIG. 12. Regional breakdown for the composite time series of large-scale mean (a) FT moisture convergence (solid) and vertical moisture transport at cloud base (dotted) (mm h^{-1}), (b) FT DSE convergence (solid) and vertical DSE transport at cloud base (dotted) (kW m^{-2}), (c) SC divergence (10^{-5} s^{-1}), and (d) precipitation with sign reversed (solid, labeled on left) and evaporation (dotted, labeled on right) (mm h^{-1}). Four oceanic basins (Indian, western Pacific, eastern Pacific, and Atlantic Oceans) are separated by color as indicated at the top. Only the highly organized systems category is shown.

fundamental properties of cloud systems within the highly organized systems category are common to all the regions studied. It is inferred that rainfall of a similar intensity accompanies a slightly stronger SC convergence in the eastern Pacific compared to other tropical oceans. Such regionality is obscure in the moisture budget because an excess of SC wind convergence in the eastern Pacific is offset by a lower evaporation rate there (Fig. 12d). The sensible heat flux is too weak in the first place to counteract the dynamic forcing in the DSE balance.

d. SC reevaporation

Reevaporation from rain falling within the subcloud layer has been assumed to be absent but should be taken into account in general. The impact of a finite SC reevaporation on the moisture and thermal budget is examined in this section.

Risi et al. (2008) showed in their Fig. 4 that reevaporation within the subcloud layer accounts for 1% of the SC moisture sources in the tropics. Bacmeister et al. (2006) demonstrated in a variety of model experiments

that the fractional reevaporation, or the vertically integrated reevaporation normalized by surface rain rate, ranges from much below 1 to as high as 2 over tropical oceans. A large portion of this reevaporation, however, occurs above cloud base. Bacmeister et al. (2006) also showed that reevaporation moistening is roughly homogeneous over height (except for a sharp minimum near the boundary layer top) from the surface to 600 hPa, beyond which it smoothly decreases upward until it vanishes around 200 hPa. Given the SC thickness of $\sim(25\text{--}50)$ hPa (Fig. 11), it is crudely estimated that SC reevaporation moistening constitutes 5%–10% of the total reevaporation throughout the troposphere. The estimates above together imply that the SC reevaporation efficiency α_{SC} defined by (24) varies from near zero to about 0.2.

Additional runs with re-evaporation rate perturbed ($\alpha_{\text{SC}} = 0.05, 0.1,$ and 0.2) are performed for highly organized systems (Fig. 13). A change to SC reevaporation modifies the vertical transport at cloud base (eddy and total) as expected from (25), (26), (35), and (36), while horizontal convergence and large-scale mean updraft

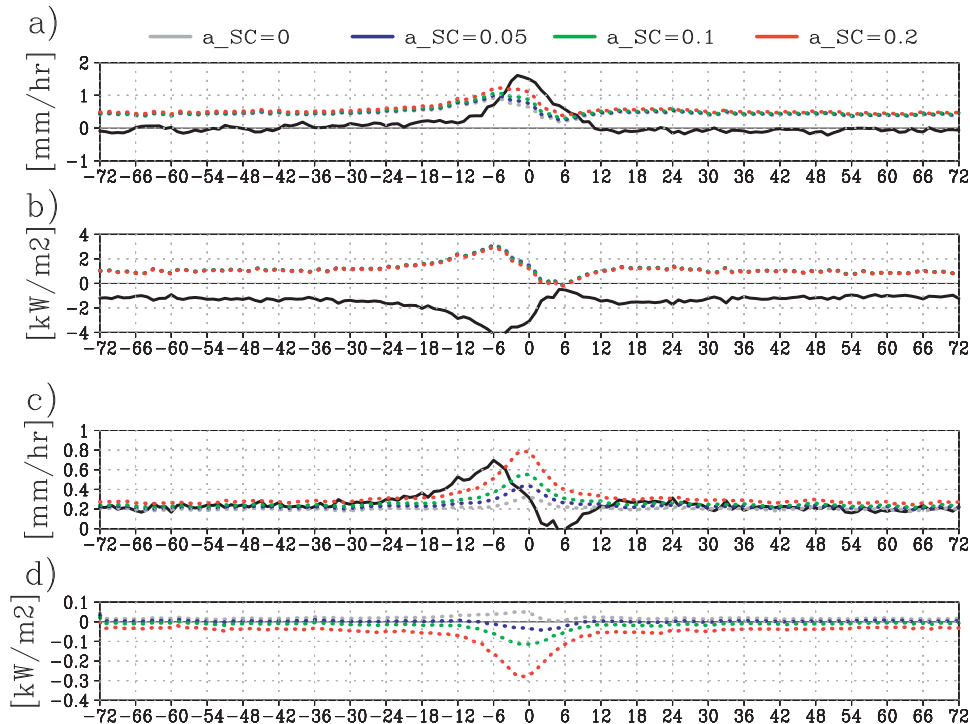


FIG. 13. The composite time series with various SC reevaporation rates for large-scale mean (a) FT moisture convergence (solid) and vertical moisture transport at cloud base (dotted) (mm h^{-1}), (b) FT DSE convergence (solid) and vertical DSE transport at cloud base (dotted) (kW m^{-2}), (c) large-scale mean moisture updraft (solid) and vertical eddy moisture transport (dotted) at cloud base (mm h^{-1}), and (d) large-scale DSE updraft (solid) and vertical eddy DSE transport (dotted) at cloud base (kW m^{-2}). Different values of α_{SC} (0, 0.05, 0.1, and 0.2) are separated by color as indicated at the top. Parameters independent of SC reevaporation are drawn in black. Only the highly organized systems category is shown.

(black lines in Fig. 13) remain unaffected. Vertical moisture transport at cloud base somewhat enhances as α_{SC} increases during a half day around when convection develops (Fig. 13a). The dependence of vertical moisture transport on α_{SC} arises from its eddy component, as depicted in Fig. 13c. Eddy moisture transport increases in magnitude rapidly with α_{SC} , because an additional SC moistening from reevaporation must be balanced out by a larger eddy moisture export through cloud base under the observational constraint (35). The enhanced eddy moistening, however, remains temporally confined to the vicinity of time zero, so that the FT moisture source several hours in advance of deep convection is still owing to large-scale mean updraft. It is not until large-scale mean moisture updraft turns to weaken (after -6 h) that eddy moisture flux could dominate large-scale mean vertical motion. In addition, lateral moisture convergence overwhelms the entire cloud-base moisture flux during ± 6 h (Fig. 13a) regardless of SC reevaporation rate perturbed within a reasonable range.

In the thermal budget, an increase of SC reevaporation lowers eddy DSE transport at cloud base so as to compensate for the evaporative cooling. As a result,

a positive (but very small) eddy DSE flux in the no-reevaporation case changes its sign to negative when even a slightest SC reevaporation ($\alpha_{\text{SC}} = 0.05$) exists. Such changes in eddy DSE flux, however, are still too weak to introduce an appreciable impact on the total vertical transport of DSE (Fig. 13b).

6. Conclusions

A composite analysis scheme proposed by Masunaga (2012a) is extended in this paper to evaluate large-scale (~ 100 km) mean thermodynamic fields before and after convective development over tropical oceans. Cloud-cleared infrared soundings are augmented by semi-theoretical in-cloud estimates derived with the aid of cloud radar and microwave radiometer measurements. The resulting composite anomalies of vapor mixing ratio and DSE show a systematic variability closely parallel with previous studies. These large-scale means are ingested to a heat and water budget analysis, where the troposphere is represented by a two-layer model constituted of the free troposphere and well-mixed subcloud layer. This simplified approach enables the diagnosis of

the FT convergence and vertical transport at cloud base of moisture and DSE with satellite observations alone.

The main findings and implications are summarized as follows.

- 1) Rainfall from isolated cumuli is overall balanced against local evaporation, while it is large-scale mean moisture convergence that feeds precipitation from organized convective systems.
- 2) Vertical moisture transport at cloud base is the dominant source of FT moistening as long as isolated cumuli prevail without deep convection nearby. In contrast, the vertical moisture flux is overwhelmed by horizontal moisture convergence during the times when highly organized systems develop. FT diabatic heating is, to a large extent, immediately cancelled out, as expected.
- 3) FT moistening by convective eddies amounts to half of the total moisture transport through cloud base in the background state, while large-scale mean updraft is mainly responsible for the modulation of cloud-base moisture flux during a few days preceding the development of highly organized systems. Eddy moisture flux at cloud base could be significantly enhanced if reevaporation moistening is efficient in the subcloud layer, although this effect is temporally limited to near the time of peak convection. The congestus “preconditioning” effect on a daily or sub-daily time scale is thus primarily attributed to large-scale mean moisture updraft rather than brought by convective eddy moistening.
- 4) The SC cooling and moistening preceding convection lower cloud base, leading to a thinning of the subcloud layer by 20 hPa when highly organized systems develop. The decrease of cloud-base height would reduce the convective inhibition and presumably facilitate the onset of convection.

Acknowledgments. The author is grateful to Scott Powell and two anonymous reviewers for their helpful comments and suggestions. The TRMM PR (2A25) dataset was provided by the Japan Aerospace Exploration Agency (JAXA), the GPROF 2010 precipitation product by Colorado State University (rain.atmos.colostate.edu/RAINMAP10), the AMSR-E CWV and SST product by Remote Sensing Systems (www.remss.com), the *CloudSat* 2B-CLDCLASS and 2B-FLXHR datasets by the CloudSat Data Processing Center (www.cloudsat.cira.colostate.edu), QuikSCAT SeaWinds ocean wind vector data by the Physical Oceanography Distributed Active Archive Center (PO.DAAC) at the NASA Jet Propulsion Laboratory (podaac.jpl.nasa.gov), and the AIRS/AMSU product by Goddard Earth

Sciences (GES) Data and Information Services Center (DISC) (disc.sci.gsfc.nasa.gov). This work is supported by the Ministry of Education, Culture, Sports, Science, and Technology (MEXT) Grant-in-Aid for Young Scientists No. 23740351.

APPENDIX

Error Analysis

The water and thermal budget parameters derived in this work are subject to random error and systematic bias originating from different sources of uncertainty. The error sources include the instrumental noise and retrieval errors inherent in individual satellite observations as well as additional uncertainties resulting from our own assumptions made. While it is impractical to build a complete error propagation model to thoroughly examine the analysis procedure, a crude error analysis simply combining known uncertainties intrinsic to original satellite data products is feasible and useful. A quick quality assessment along this line is carried out in this appendix.

The QuikSCAT wind has a root-mean-square (rms) error less than 1 m s^{-1} and a bias of 0.1 m s^{-1} at most, except for very rare occasions with extremely high winds (Ebuchi et al. 2002; Bourassa et al. 2003; Fangohr and Kent 2012). These values are adopted for the error estimates of evaporation and SC convergence. SST uncertainties from AMSR-E observations are quite small over tropical oceans (an rms error of $<1 \text{ K}$ with virtually zero bias) (Gentemann et al. 2010) and practically would not affect the evaporation estimates. The relative rms error in AMSR-E oceanic precipitation is about 200% at a rain rate of 0.2 mm h^{-1} (Lin and Hou 2008), and the relative precipitation bias varies from -5% to -17% , depending on the ground stations compared (Wolff and Fisher 2009). Precipitation uncertainties are estimated here to have a random error twice as large as the background level and a negative bias of 15%.

L’Ecuyer et al. (2008) assessed the *CloudSat* radiative flux product and found the rms errors (biases) of 4.4 (0.03), 26.7 (5.5), 11.5 (13.2), and 15.2 (16.1) W m^{-2} for outgoing longwave, outgoing shortwave, downwelling surface longwave, and downwelling surface shortwave fluxes, respectively, against the Clouds and the Earth’s Radiant Energy System (CERES) Fast Longwave and Shortwave Radiative Fluxes (FLASHFlux) data.^{A1} These numbers amount to the rms error of 33.1 W m^{-2} and the

^{A1} Note that surface flux estimates from the CERES FLASH-Flux product are analyzed from satellite measurements and are not strictly the “ground truth.”

TABLE A1. Error statistics for the budget analysis. Numbers in parentheses are the relative percentages normalized by the background level.

	\bar{E} (mm h ⁻¹)	\bar{P}_s (mm h ⁻¹)	$\overline{\langle \mathbf{V} \cdot q \mathbf{v} \rangle}_{SC}$ (mm h ⁻¹)	$\overline{\langle Q_R \rangle}$ (kW m ⁻²)	$\overline{\langle \mathbf{V} \cdot s \mathbf{v} \rangle}_{SC}$ (kW m ⁻²)
Standard error	2.7×10^{-5} (0.014%)	2.9×10^{-4} (0.13%)	9.9×10^{-5} (0.062%)	2.1×10^{-4} (0.22%)	1.0×10^{-4} (0.014%)
Bias	3.1×10^{-3} (1.5%)	-3.5×10^{-2} (-15%)	2.5×10^{-3} (1.5%)	-3.5×10^{-2} (36%)	1.1×10^{-2} (1.5%)
Background	0.20	0.23	0.16	-0.097	0.76

bias of -34.8 W m^{-2} for $\overline{\langle Q_R \rangle}$. AIRS air temperature at the lowermost level has a relative rms error of 1.5 K and a bias of -0.5 K (Susskind et al. 2011). Susskind et al. (2011) evaluated the relative rms error of AIRS water vapor to be about 10% in the lowermost layer, but did not mention the water vapor bias in that layer. Since their estimate of the total precipitable water bias is as small as -0.06 cm , we assume here that the near-surface water vapor bias is also practically negligible. These temperature and water vapor uncertainties are used for evaluating SC moisture and DSE convergence errors together with the QuikSCAT wind uncertainty.

Random errors associated with instantaneous satellite retrievals would be largely cancelled out when averaged into composite time series. For the current analysis, the sample size is $O(10^6)$ for the QuikSCAT and AMSR-E parameters, $O(10^4-10^5)$ for the AIRS variables, and $O(10^4)$ for the *CloudSat* data, with the numerical factor varying over time in composite space. The standard error, that is, individual rms errors divided by the square root of the sample size, is computed for the error statistics shown next as a measure of the robustness of composite means.

Table A1 summarizes the estimated uncertainties for selected budget parameters. Other variables are secondary estimates derived with the budget equations and are not listed. It is noted that the large-scale mean moisture and DSE transports at cloud base, that is, $\bar{q}_{CB}\bar{\omega}_{CB}/g$ and $\bar{s}_{CB}\bar{\omega}_{CB}/g$, are virtually equivalent to the SC convergence [see (33) and (34)] and have been omitted from the table to avoid redundancy. Standard errors listed in Table A1 are computed with the minimum sample size (i.e., the worst case) in the whole composite time series, which typically occurs near time zero for highly organized systems. Also presented in parentheses are the relative values normalized by the background level of each parameter. The background values, shown in the bottom row of Table A1, are defined as the first and last 12-h time series averaged together from the isolated cumulus composite. The standard error is found to be consistently small.

Systematic biases, in contrast, do not reduce as the sample size increases and can be much larger. Precipitation

rate has a negative bias of 0.035 mm h^{-1} (or 15% of the background as noted above), and the column-integrated radiative heating suffers from a cooling bias of 0.035 kW m^{-2} (the relative bias of 36%). The radiative cooling bias is seemingly large but is not critical for the thermal budget analysis, where the magnitude of $\langle Q_R \rangle$ itself stays constantly minor. Care must be taken when a quantitative assessment is attempted on a subtle budget imbalance, although any of those bias estimates are not so severe as to question the major conclusions discussed in this paper. The relative bias of other budget parameters is as small as 1%–2%.

Other uncertainty sources that potentially affect the current budget analysis include diurnal sampling bias. The composite parameters are evaluated from sun-synchronous satellite measurements and can be biased to a certain phase of diurnal cycle. This problem may be even more complicated by the fact that A-Train and QuikSCAT overpasses are 4.5 h apart in local time. The diurnal variation associated with tropical disturbances is generally modest over ocean, with the relative magnitude of 14% for rainfall (Imaoka and Spencer 2000) and 30% for surface divergence (Deser 1994). The actual diurnal bias in the present analysis would be much smaller than these values since the opposite phases of diurnal variation would be largely averaged out between ascending and descending satellite paths, leaving behind only a small residual ascribed to higher-order diurnal harmonics.

Finally, in situ measurements documented in past work are briefly compared with the current analysis for an independent verification. Thompson et al. (1979) applied tropical Atlantic field experiment data to a tropospheric budget analysis and found that $P_s = 12.5 \text{ mm day}^{-1}$ (0.52 mm h^{-1}), $E = 3.8 \text{ mm day}^{-1}$ (0.16 mm h^{-1}), and moisture convergence is 9.5 mm day^{-1} (0.40 mm h^{-1}) on average, while $P_s = 22.0 \text{ mm day}^{-1}$ (0.92 mm h^{-1}), $E = 4.1 \text{ mm day}^{-1}$ (0.17 mm h^{-1}), and moisture convergence is 19.4 mm day^{-1} (0.81 mm h^{-1}) during a passage of trough. These values not only fit within the range between the background state and convective peak given by Fig. 5, but also support the aforementioned finding that precipitation and moisture convergence vary

concurrently and roughly cancel each other while evaporation stays small. As for the thermal budget, $LP_s = 0.357 \text{ kW m}^{-2}$, $S = 0.012 \text{ kW m}^{-2}$, and DSE convergence is -0.284 kW m^{-2} on average, and $LP_s = 0.629 \text{ kW m}^{-2}$, $S = 0.018 \text{ kW m}^{-2}$, and DSE convergence is -0.597 kW m^{-2} during a trough (Thompson et al. 1979). Similarly to the moisture budget, these estimates reasonably agree with the present outcomes in Fig. 6.

The vertical eddy transport of moist static energy (MSE) at cloud base,

$$-\left. \frac{\overline{h'\omega'}}{g} \right|_{\text{CB}} = -\left. \frac{\overline{s'\omega'} + L\overline{q'\omega'}}{g} \right|_{\text{CB}}, \quad (\text{A1})$$

is estimated from the present results to be $0.15\text{--}0.18 \text{ kW m}^{-2}$ for all three composite categories when averaged over time from -24 h to $+24 \text{ h}$. These numbers are in reasonable agreement with the estimate by Yanai et al. (1973), who showed in their Fig. 11 that the lower tropospheric vertical eddy flux of MSE reads about $370 \text{ cal cm}^{-2} \text{ day}^{-1}$ or 0.18 kW m^{-2} . Equation (A1) may be approximated using (35) and (36) by

$$-\left. \frac{\overline{h'\omega'}}{g} \right|_{\text{CB}} \approx L\overline{E} + \overline{S} + \overline{\langle Q_R \rangle}_{\text{SC}}.$$

It is suggested that the vertical eddy flux of MSE at cloud base is mainly determined by surface latent heat flux $L\overline{E}$, with the other two terms in the right-hand side together being an order of magnitude smaller over ocean.

REFERENCES

- Arakawa, A., and W. H. Schubert, 1974: Interaction of a cumulus cloud ensemble with the large-scale environment. Part I. *J. Atmos. Sci.*, **31**, 674–701.
- Bacmeister, J. T., M. J. Suarez, and F. R. Robertson, 2006: Rain reevaporation, boundary layer-convection interactions, and Pacific rainfall patterns in an AGCM. *J. Atmos. Sci.*, **63**, 3383–3403.
- Bourassa, M. A., D. M. Legler, J. J. O'Brien, and S. R. Smith, 2003: SeaWinds validation with research vessels. *J. Geophys. Res.*, **108**, 3019, doi:10.1029/2001JC001028.
- Brown, R. G., and C. D. Zhang, 1997: Variability of midtropospheric moisture and its effect on cloud-top height distribution during TOGA COARE. *J. Atmos. Sci.*, **54**, 2760–2774.
- Chen, S. S., and R. A. Houze Jr., 1997: Diurnal variation and lifecycle of deep convective systems over the tropical Pacific warm pool. *Quart. J. Roy. Meteor. Soc.*, **123**, 357–388.
- Derbyshire, S. H., I. Beau, P. Bechtold, J. Y. Grandpeix, J. M. Piriou, J. L. Redelsperger, and P. M. M. Soares, 2004: Sensitivity of moist convection to environmental humidity. *Quart. J. Roy. Meteor. Soc.*, **130**, 3055–3079.
- Deser, C., 1994: Daily surface wind variations over the equatorial Pacific Ocean. *J. Geophys. Res.*, **99**, 23 071–23 078.
- Ebuchi, N., H. C. Graber, and M. J. Caruso, 2002: Evaluation of wind vectors observed by QuikSCAT/SeaWinds using ocean buoy data. *J. Atmos. Oceanic Technol.*, **19**, 2049–2062.
- Emanuel, K. A., 1995: The behavior of a simple hurricane model using a convective scheme based on subcloud-layer entropy equilibrium. *J. Atmos. Sci.*, **52**, 3960–3968.
- Fangohr, S., and E. Kent, 2012: An estimate of structural uncertainty in QuikSCAT wind vector retrievals. *J. Appl. Meteor. Climatol.*, **51**, 954–961.
- Gentemann, C. L., T. Meissner, and F. J. Wentz, 2010: Accuracy of satellite sea surface temperatures at 7 and 11 GHz. *IEEE Trans. Geosci. Remote Sens.*, **48**, 1009–1018.
- Hohenegger, C., and B. Stevens, 2013: Preconditioning deep convection with cumulus congestus. *J. Atmos. Sci.*, **70**, 448–464.
- Holloway, C. E., and J. D. Neelin, 2009: Moisture vertical structure, column water vapor, and tropical deep convection. *J. Atmos. Sci.*, **66**, 1665–1683.
- Imaoka, K., and R. W. Spencer, 2000: Diurnal variation of precipitation over the tropical oceans observed by TRMM/TMI combined with SSM/I. *J. Climate*, **13**, 4149–4158.
- Johnson, R. H., 1976: Role of convective-scale precipitation downdrafts in cumulus and synoptic-scale interactions. *J. Atmos. Sci.*, **33**, 1890–1910.
- , T. M. Rickenbach, S. A. Rutledge, P. E. Ciesielski, and W. H. Schubert, 1999: Trimodal characteristics of tropical convection. *J. Climate*, **12**, 2397–2418.
- Kemball-Cook, S. R., and B. C. Weare, 2001: The onset of convection in the Madden-Julian oscillation. *J. Climate*, **14**, 780–793.
- Kondo, Y., A. Higuchi, and K. Nakamura, 2006: Small-scale cloud activity over the Maritime Continent and the western Pacific as revealed by satellite data. *Mon. Wea. Rev.*, **134**, 1581–1599.
- Kuang, Z., and C. S. Bretherton, 2006: A mass-flux scheme view of a high-resolution simulation of a transition from shallow to deep cumulus convection. *J. Atmos. Sci.*, **63**, 1895–1909.
- Kummerow, C. D., W. Barnes, T. Kozu, J. Shiue, and J. Simpson, 1998: The Tropical Rainfall Measuring Mission (TRMM) sensor package. *J. Atmos. Oceanic Technol.*, **15**, 809–817.
- , and Coauthors, 2001: The evolution of the Goddard Profiling Algorithm (GPROF) for rainfall estimation from passive microwave sensors. *J. Appl. Meteor.*, **40**, 1801–1820.
- Large, W. G., J. C. McWilliams, and S. C. Doney, 1994: Oceanic vertical mixing: A review and a model with a nonlocal boundary layer parameterization. *Rev. Geophys.*, **32**, 363–403.
- L'Ecuyer, T. S., and G. L. Stephens, 2003: The tropical oceanic energy budget from the TRMM perspective. Part I: Algorithm and uncertainties. *J. Climate*, **16**, 1967–1985.
- , N. B. Wood, T. Haladay, G. L. Stephens, and P. W. Stackhouse Jr., 2008: Impact of clouds on atmospheric heating based on the R04 CloudSat fluxes and heating rates data set. *J. Geophys. Res.*, **113**, D00A15, doi:10.1029/2008JD009951.
- Lin, X., and R. H. Johnson, 1996: Heating, moistening, and rainfall over the western Pacific warm pool during TOGA COARE. *J. Atmos. Sci.*, **53**, 3367–3383.
- , and A. Y. Hou, 2008: Evaluation of coincident passive microwave rainfall estimates using TRMM PR and ground measurements as references. *J. Appl. Meteor. Climatol.*, **47**, 3170–3187.
- Luo, H., and M. Yanai, 1984: The large-scale circulation and heat sources over the Tibetan Plateau and surrounding areas during the early summer of 1979. Part II: Heat and moisture budgets. *Mon. Wea. Rev.*, **112**, 966–989.
- Mapes, B., 1997: Equilibrium vs. activation controls on large-scale variations of tropical deep convection. *The Physics and*

- Parameterization of Moist Atmospheric Convection*, R. K. Smith, Ed., Kluwer Academic Publishers, 321–358.
- , S. Tulich, J. Lin, and P. Zuidema, 2006: The mesoscale convection life cycle: Building block or prototype for large-scale tropical waves? *Dyn. Atmos. Oceans*, **42**, 3–29.
- , R. Milliff, and J. Morzel, 2009: Composite life cycle of maritime tropical mesoscale convective systems in scatterometer and microwave satellite observations. *J. Atmos. Sci.*, **66**, 199–208.
- Masunaga, H., 2012a: A satellite study of the atmospheric forcing and response to moist convection over tropical and subtropical oceans. *J. Atmos. Sci.*, **69**, 150–167.
- , 2012b: Short-term versus climatological relationship between precipitation and tropospheric humidity. *J. Climate*, **25**, 7983–7990.
- , and C. D. Kummerow, 2006: Observations of tropical precipitating clouds ranging from shallow to deep convective systems. *Geophys. Res. Lett.*, **33**, L16805, doi:10.1029/2006GL026547.
- Nitta, T., and S. Esbensen, 1974: Heat and moisture budget analyses using BOMEX data. *Mon. Wea. Rev.*, **102**, 17–28.
- Numaguti, A., R. Oki, K. Nakamura, K. Tsuboki, N. Misawa, T. Asai, and Y. M. Kodama, 1995: 4–5-day-period variation and low-level dry air observed in the equatorial western Pacific during the TOGA-COARE IOP. *J. Meteor. Soc. Japan*, **73**, 267–290.
- Perry, K. L., 2001: SeaWinds on QuikSCAT level 3 daily, gridded ocean wind vectors (JPL SeaWinds project) version 1.1. JPL Doc. D-20335, Jet Propulsion Laboratory, Pasadena, California, 39 pp. [Available online at <http://podaac.jpl.nasa.gov>.]
- Rasmussen, K. L., and R. A. Houze Jr., 2011: Orographic convection in subtropical South America as seen by the TRMM satellite. *Mon. Wea. Rev.*, **139**, 2399–2420.
- Raymond, D. J., 1995: Regulation of moist convection over the west Pacific warm pool. *J. Atmos. Sci.*, **52**, 3945–3959.
- , 2000: Thermodynamic control on tropical rainfall. *Quart. J. Roy. Meteor. Soc.*, **126**, 889–898.
- , and S. L. Sessions, 2007: Evolution of convection during tropical cyclogenesis. *Geophys. Res. Lett.*, **34**, L06811, doi:10.1029/2006GL028607.
- Reed, R. J., and E. E. Recker, 1971: Structure and properties of synoptic-scale wave disturbances in the equatorial western Pacific. *J. Atmos. Sci.*, **28**, 1117–1133.
- Riehl, H., and J. S. Malkus, 1958: On the heat balance in the equatorial trough zone. *Geophysica*, **6**, 503–538.
- Risi, C., S. Bony, and F. Vimeux, 2008: Influence of convective processes on the isotopic composition ($\delta^{18}\text{O}$ and δD) of precipitation and water vapor in the tropics: 2. Physical interpretation of the amount effect. *J. Geophys. Res.*, **113**, D19306, doi:10.1029/2008JD009943.
- Romatschke, U., and R. A. Houze Jr., 2010: Extreme summer convection in South America. *J. Climate*, **23**, 3761–3791.
- Sherwood, S. C., 1999: Convective precursors and predictability in the tropical western Pacific. *Mon. Wea. Rev.*, **127**, 2977–2991.
- , and R. Wahrlich, 1999: Observed evolution of tropical deep convective events and their environment. *Mon. Wea. Rev.*, **127**, 1777–1795.
- Short, D. A., and K. Nakamura, 2000: TRMM radar observations of shallow precipitation over the tropical oceans. *J. Climate*, **13**, 4107–4124.
- Straub, K. H., and G. N. Kiladis, 2003: The observed structure of convectively coupled Kelvin waves: Comparison with simple models of coupled wave instability. *J. Atmos. Sci.*, **60**, 1655–1668.
- Susskind, J., C. D. Barnett, and J. M. Blaisdell, 2003: Retrieval of atmospheric and surface parameters from AIRS/AMSU/HSB data in the presence of clouds. *IEEE Trans. Geosci. Remote Sens.*, **41**, 390–409.
- , J. M. Blaisdell, L. Iredell, and F. Keita, 2011: Improved temperature sounding and quality control methodology using AIRS/AMSU data: The AIRS science team version 5 retrieval algorithm. *IEEE Trans. Geosci. Remote Sens.*, **49**, 883–907.
- Takayabu, Y. N., K.-M. Lau, and C.-S. Sui, 1996: Observation of a quasi-2-day wave during TOGA COARE. *Mon. Wea. Rev.*, **124**, 1892–1913.
- Takemi, T., O. Hirayama, and C. Li, 2004: Factors responsible for the vertical development of tropical oceanic cumulus convection. *Geophys. Res. Lett.*, **31**, L11109, doi:10.1029/2004GL020225.
- Tao, W.-K., and Coauthors, 2006: Retrieval of latent heating from TRMM measurements. *Bull. Amer. Meteor. Soc.*, **87**, 1555–1572.
- Thompson, R. M., S. W. Payne, E. E. Recker, and R. J. Reed, 1979: Structure and properties of synoptic-scale wave disturbances in the intertropical convergence zone of the eastern Atlantic. *J. Atmos. Sci.*, **36**, 53–72.
- TRMM PR Team, 2005: Tropical Rainfall Measuring Mission (TRMM) precipitation radar algorithm: Instruction manual for version 6. Japan Aerospace Exploration Agency and National Aeronautics and Space Administration, 175 pp. [Available online at http://www.eorc.jaxa.jp/TRMM/document/pr_manual/pr_manual_v6.pdf.]
- Waite, M. L., and B. Khouider, 2010: The deepening of tropical convection by congestus preconditioning. *J. Atmos. Sci.*, **67**, 2601–2615.
- Wang, Z., and K. Sassen, 2001: Cloud type and macrophysical property retrieval using multiple remote sensors. *J. Appl. Meteor.*, **40**, 1665–1682.
- Wentz, F. J., and T. Meissner, 2000: AMSR ocean algorithm. Algorithm Theoretical Basis Doc., Remote Sensing Systems, Santa Rosa, California, 59 pp.
- Wolff, D. B., and B. L. Fisher, 2009: Assessing the relative performance of microwave-based satellite rain-rate retrievals using TRMM ground validation data. *J. Appl. Meteor. Climatol.*, **48**, 1069–1099.
- Yanai, M., S. Esbensen, and J.-H. Chu, 1973: Determination of bulk properties of tropical cloud clusters from large-scale heat and moisture budgets. *J. Atmos. Sci.*, **30**, 611–627.
- Yoneyama, K., and T. Fujitani, 1995: The behavior of dry westerly air associated with convection observed during the TOGA-COARE R/V Natsushima cruise. *J. Meteor. Soc. Japan*, **73**, 291–304.
- Zelinka, M. D., and D. L. Hartmann, 2009: Response of humidity and clouds to tropical deep convection. *J. Climate*, **22**, 2389–2404.
- Zipser, E. J., 1969: The role of organized unsaturated convective downdrafts in the structure and rapid decay of an equatorial disturbance. *J. Appl. Meteor.*, **8**, 799–814.
- , 1977: Mesoscale and convective-scale downdrafts as distinct components of squall-line structure. *Mon. Wea. Rev.*, **105**, 1568–1589.